DRDC Tracking Number E15-0202-1137 Final Publication Number DRDC-RDDC-2015-P063

A revised manuscript submitted to *Int. J. Heat Fluid Flow* (HFF-D-15-00059R2)

Study of the Interference of Plumes Released from Two Near-Ground Point Sources in an Open Channel

Shahin N. Oskouie[a], Bing-Chen Wang[a] * and Eugene Yee[b]

[a] *Dept. of Mechanical Engineering, Univ. of Manitoba, Winnipeg, MB, R3T 5V6, Canada*

[b] *Defence R&D Canada, Suffield Research Centre, P.O. Box 4000, Stn Main, Medicine Hat, AB, T1A 8K6, Canada*

Abstract

The dispersion and mixing of passive scalars released from two near-ground point sources into an open-channel flow are studied using direct numerical simulation. A comparative study based on eight test cases has been conducted to investigate the effects of Reynolds number and source separation distance on the dispersion and interference of the two plumes. In order to determine the nonlinear relationship between the variance of concentration fluctuations of the total plume and those produced by each of the two plumes, the covariance of the two concentration fields is studied in both physical and spectral spaces. The results show that at the source height, the streamwise evolution of the cross correlation between the fluctuating components of the two concentration fields can be classified into four stages, which feature zero, destructive and constructive interferences and a complete mixing state. The characteristics of these four stages of plume mixing are further confirmed through an analysis of the pre-multiplied co-spectra and coherency spectra. From the coherency spectrum, it is observed that there exists a range of 'leading scales', which are several times larger than the Kolmogorov scale but are smaller than or comparable to the scale of the most energetic eddies of turbulence. At the leading scales, the mixing between the two interfering plumes is the fastest and the coherency spectrum associated with these scales can quickly approach its asymptotic value of unity.

Key words: Plume interference, dispersion, passive scalar, boundary layer, turbulence.

* Corresponding author. Email: BingChen.Wang@Ad.Umanitoba.Ca
Tel: +1 (204) 474-9305, Fax: +1 (204) 275-7507.

In revision: 23 July 2015

NOMENCLATURE

c	instantaneous concentration
C	mean concentration
$Co_{c'_A c'_B}$	co-spectrum of concentration fluctuations
d	source separation distance
$E_{c'c'}$	power spectrum of concentration fluctuations
$E_{w'w'}$	power spectrum of spanwise velocity fluctuations
f	frequency
f^*	non-dimensionalized frequency: $f\delta/u_\tau$
k	wavenumber
L	channel length
M	meandering ratio: σ_c^2/σ_r^2
N	number of grid nodes
p	pressure
r	local ratio of the upstream to downstream gradient in the concentration field
Re_τ	Reynolds number based on the wall friction velocity: $u_\tau\delta/\nu$
Sc	Schmidt number: ν/α
t	time
T	temporal interval: δ/u_τ
u	velocity component in the streamwise direction
u_i	velocity components: $i = 1, 2, 3$
u_τ	wall friction velocity
U	mean velocity in the streamwise direction
v	velocity component in the wall-normal direction
w	velocity component in the spanwise direction
x_i	coordinates: $i = 1, 2, 3$
z_c	instantaneous plume centroid

Greek Symbols:

α	molecular diffusivity of the scalar
δ	channel height
Δ	grid size
λ	size of turbulent eddies
ν	kinematic viscosity
ρ_{cc}	cross correlation coefficient between concentration fluctuations
ρ_{cs}	coherency spectrum
ϱ	density

σ_c	instantaneous plume centroid dispersion
σ_r	relative plume dispersion
σ_z	mean plume dispersion
Σ_r	relative plume half width
Σ_z	mean plume half width
ψ	limiter function

Subscripts:

$(\cdot)_A$	value for the plume released from source A
$(\cdot)_B$	value for the plume released from source B
$(\cdot)_m$	maximum value
$(\cdot)_{mid}$	value at the midpoint in the spanwise direction between the two plumes
$(\cdot)_r$	value in the relative frame
$(\cdot)_{rms}$	root-mean-squared quantity
$(\cdot)_s$	value at the source
$(\cdot)_T$	value for the total plume
$(\cdot)_x$, $(\cdot)_y$, $(\cdot)_z$	streamwise, wall-normal, and spanwise components, respectively
$\bar{(\cdot)}$	time-averaged quantity
$(\cdot)^+$	wall coordinates
$(\cdot)'$	fluctuating component

Abbreviations:

DNS	Direct Numerical Simulation
MPI	Message Passing Interface
TVD	Total Variation Diminishing
UMIST	Upstream Monotonic Interpolation for Scalar Transport

1 Introduction

In engineering and environmental applications, one frequently encounters turbulent dispersion and mixing of passive scalars released from multiple concentrated (point or line) sources. For instance, in atmospheric pollution, hazardous materials are often released from multiple sources that are close to each other. Also, in nature, the precise detection of the exact locations of multiple food sources using the olfactory system is critical to the survival of many predatory and non-predatory animals. In most of these applications, the dispersion of gases and vapors in the air (Schmidt number ≈ 1) is of primary interest. Also, the sources are often located at ground level, where the flow is inhomogeneous and anisotropic. This further imposes challenges to the study of the temporal and spatial development and mutual interaction of passive scalar plumes, since most of the current theoretical models available for predicting turbulent dispersion and mixing of two or more scalars have been primarily limited to homogeneous and isotropic turbulent flows.

The dispersion and interference of plumes released from two or more point sources are determined by many factors including the source sizes, length scales of the plumes and turbulent eddies, and mean and fluctuating velocities. The relative length scales of the scalar and turbulent eddies influence significantly the plume dispersion patterns. For a single plume, if the size of the plume is smaller than that of the most energetic scale of turbulent motions, the plume meanders with the flow. However, if the plume size is larger than the most energetic scale of the flow motion, the plume mixing exhibits a Brownian diffusion pattern. For the development of two and more plumes, the mechanism becomes more complicated because of plume interference and involvement of additional length scales such as source separation distances. Another challenge involved in the study of a multi-source release problem is that although the governing equation for the passive scalar is linear, the interaction of higher-order statistics of two scalar fields is typically nonlinear. Although, the first-order statistics of the total scalar (i.e., mean concentration) are linearly superposable, the second- and higher-order statistics of the total scalar (e.g., variance of concentration fluctuations) are not.

Despite the importance of the subject, studies on the interaction of passive scalars emitted from multiple concentrated sources are still rather limited in the literature. Based on wind-tunnel measurements, Warhaft (1984) investigated the interference of passive thermal fields produced by two line sources in decaying grid turbulence. He observed that the inter-

ference between the two thermal plumes may alter the total temperature variance level, and this effect varies with the separation distance between the two line sources, source position from the grid, and downstream location where the measurements were taken. Stapountzis (1988) conducted a series of wind-tunnel experiments to investigate the mixing of two passive thermal plumes generated from two line sources separated in either the spanwise or streamwise directions. He found that there was a strong negative correlation between the temperature fluctuations within the meandering regime of plume development released from two transversely separated line sources, and that the correlation coefficient became positively valued when the two line sources were aligned in the streamwise direction. Tong and Warhaft (1995) investigated the dispersion and mixing of passive scalars produced by two heated fine rings placed axisymmetrically in a turbulent jet. Their results on the coherency spectrum of concentration fluctuations of the two plumes showed that the small scales lag behind the large scales in the mixing of two plumes. Davis *et al.* (2000) studied the interaction of plumes released from two point sources into the atmospheric boundary layer. Their measurement results on two laterally separated sources showed that the correlation between the concentration fluctuations of the two plumes change from negative to positive as the downwind distance increases for a fixed source separation distance, or as the source separation distance decreases for a fixed downwind location.

Vrieling and Nieuwstadt (2003) performed direct numerical simulation (DNS) to study the interference of two nearby line sources in a plane-channel flow. They placed their line sources at the center of the channel to emulate a concentration release in homogeneous turbulence, and observed that the covariance between the two plumes depends on the spacing between the sources and the downstream distance from the sources. They also obtained an analytical expression for the combined variance of the total concentration fluctuation based on the well-known meandering plume model of Gifford (1959). With their analytical model, Vrieling and Nieuwstadt (2003) were able to compute statistics related to the interference of concentration plumes under practical atmospheric dispersion conditions where the meandering effect is strong. However, at far downstream locations where the effect of plume meandering reduces significantly, their model failed to predict the numerical results. Yee *et al.* (2003) used a meandering plume model incorporating internal fluctuations to provide explicit analytical expressions for various higher-order joint concentration statistics for plume

fluctuations arising from a two-point source release in homogeneous isotropic turbulence. The model prediction of Yee *et al.* (2003) on the second-order correlation function (cross correlation) between the concentration fluctuations were in good agreement with some experimental data for a two point source release in grid turbulence acquired in a water-channel simulation. Costa-Patry and Mydlarski (2008) conducted a wind-tunnel experiment to quantify the interaction of two scalar fields generated by two line sources (separated in the wall-normal direction) in a fully-developed high-aspect-ratio turbulent channel flow. Their results on the co-spectrum and the coherency spectrum revealed that the large scales (occurring at low frequencies) of plume mixing evolve more rapidly than the small scales (occurring at high frequencies).

Most of these experimental, numerical, and theoretical investigations are limited to the study of the dispersion and interference of plumes released from line sources in homogeneous turbulence or at vertical distances far enough from a solid surface (in plane-channel flow) where the turbulence is approximately homogeneous. However, as is mentioned above, the dispersion and interference of plumes released from concentrated point (or, compact) sources located at or near-ground level, where the mean flow and turbulence is inhomogeneous, is of greatest interest in most practical applications. In this paper, we use DNS to study the interference of passive scalars released from two near-ground level point sources in the context of a neutrally-stratified wall-bounded shear flow at two Reynolds numbers. The first- and second-order concentration statistics of the single and total plumes are analyzed, the dynamic interaction of the two plumes in a turbulent wall shear layer and the correlations between their concentration fluctuations are investigated. Furthermore, in order to develop a deeper understanding of the mixing of two plumes at different length scales, a detailed analysis based on the co-spectrum and coherency spectrum of the plumes is also performed.

The remainder of this paper is organized as follows. In section 2, the problem definition and test cases are introduced. In section 3, the numerical algorithm for performing DNS is described. In section 4, the results of the numerical simulations are presented and analyzed. Finally, in section 5, major conclusions of this research are summarized.

2 Problem Description

In this study, we considered the release of two plumes from two point sources in an open-channel flow at two Reynolds numbers for $Re_\tau \equiv u_\tau \delta/\nu = 180$ and 395. Here $\delta = 0.04$ m is the height of the open channel, u_τ is the friction velocity and ν is the kinematic viscosity of the fluid. Figure 1 shows a schematic of the computational domain, which extends $4\pi\delta \times \delta \times 4/3\pi\delta$ for $Re_\tau = 180$ and $2\pi\delta \times \delta \times \pi\delta$ for $Re_\tau = 395$ in the streamwise (x), vertical (y) and spanwise (z) directions, respectively. The two point sources labeled 'A' and 'B' in figure 1 are positioned symmetrically in the spanwise (z) direction with respect to the centerline of the open channel. The two sources are of equal strength and are positioned vertically at $y_s^+ \equiv y_s u_\tau/\nu = 5$ above the lower wall. As such, both point sources are within the viscous sublayer, corresponding to a near-ground level release condition. The effects of source separation d on the interference of plumes can be significantly influenced by the Reynolds number. In order to investigate this coupled mechanism, 8 different test cases are considered. Table 1 summarizes the Reynolds numbers and source separation distances tested. Related to the grid resolution for DNS, the source sizes used for the two different Reynolds numbers are also given in the table.

3 Numerical Algorithm

For DNS, the continuity equation, momentum equations and transport equation of a passive scalar take the following forms for an incompressible fluid flow:

$$\frac{\partial u_i}{\partial x_i} = 0, \tag{1}$$

$$\frac{\partial u_i}{\partial t} + u_j \frac{\partial u_i}{\partial x_j} = -\frac{1}{\varrho}\frac{\partial p}{\partial x_i} + \nu \frac{\partial^2 u_i}{\partial x_j \partial x_j}, \tag{2}$$

$$\frac{\partial c}{\partial t} + u_j \frac{\partial c}{\partial x_j} = \alpha \frac{\partial^2 c}{\partial x_j \partial x_j}, \tag{3}$$

where u_i, p and c represent the velocity, pressure and concentration fields, respectively; ϱ is the density of the fluid; and α represents the molecular diffusivity of the scalar. In this study, the Schmidt number $Sc = \nu/\alpha$ is equal to 1. In the above equations, x_i represents coordinates (for $i = 1$, 2 and 3), corresponding to the streamwise x, vertical y, and spanwise z directions, respectively.

The DNS was conducted using an in-house code developed using the FORTRAN 90/95 programming language and fully-parallelized using the message passing interface (MPI) li-

brary. Numerical simulations were conducted on the Western Canada Research Grid (Westgrid), which encompasses 15 partner institutions and is one of four consortia that provides high-performance computational resources across Canada. The total computing time spent on solving the flow and scalar fields and on collecting the statistics is over 16,000 and 80,000 CPU hours for $Re_\tau = 180$ and 395, respectively.

The momentum equations were discretized using the fully-conservative energy-conserving second-order finite difference method of Ham *et al.* (2002) based on a non-uniform staggered grid system. A fully implicit four-level fractional step method of Choi and Moin (1994) coupled with a second-order Crank-Nicolson scheme was used to advance the velocity field over a single time step. The diffusion term in the momentum equations was discretized using a central-differencing scheme. For pressure correction at each time step, a Poisson equation (derived from the continuity equation) was solved using a multigrid method.

The advection-diffusion equation that governs the transport of the passive scalar c was solved after the solution of the momentum equations at each time step. It should be noted that the advection-diffusion equation for the scalar was solved twice at each time step, once each for sources A and B. The simulations were executed until statistically stationary conditions were attained for both velocity and concentration fields, after which various statistics of both individual and total concentration fields from the two sources were collected over a time period of $50T$, where $T \equiv \delta/u_\tau$.

Owing to the presence of high gradients in the instantaneous concentration fields, it is critically important to use a proper numerical scheme for the discretization of the convective term in the advection-diffusion equation of the scalar. It is known that if a second-order central-differencing scheme is used for the discretization of the convective term, non-physical oscillations may occur in the solution for c which can result in unphysical negative concentrations. On the other hand, the use of an upwind scheme may "smear out" the plume concentration field owing to the large numerical diffusion inherent in this scheme. These problems have been identified and discussed previously by Brethouwer *et al.* (1999), Livescu *et al.* (2000), Vrieling and Nieuwstadt (2003), Xie *et al.* (2004) and Boppana *et al.* (2012). Based on the previous experience of these investigators, we used a total variation diminishing (TVD) scheme to discretize the convective term in the advection-diffusion equation. TVD schemes are monotonicity preserving, and as a consequence, do not result in non-physical

oscillations in the concentration field. In particular, the instantaneous concentration obtained as a solution of the advection-diffusion equation should always remain non-negative and never exceed the source concentration level (maximum realizable concentration level). To this purpose and based on a comparative study of Waterson and Deconinck (2007), the Sharp and Monotonic Algorithm for Realistic Transport (SMART) developed by Gaskell and Lau (1988) is used to discretize the convective term in the advection-diffusion equation for the scalar. The SMART scheme has the following limiter function:

$$\phi(r) = \max\left[0, \min\left(2r, \frac{3r+1}{4}, 4\right)\right] \tag{4}$$

where $\phi(r)$ is the limiter function and r is the local ratio of the upstream gradient to downstream gradient in the concentration field. The SMART scheme is essentially third-order accurate, however, it reduces to an upwind and a central differencing scheme for $\psi(r) = 0$ and 1, respectively.

For the velocity field, we applied periodic boundary conditions in the streamwise and spanwise directions, a no-slip boundary condition on the bottom wall, and a free-slip boundary condition along the top surface of the computational domain. For the concentration field, a zero Dirichlet condition was applied at the inlet boundary, and zero Neumann conditions were applied at the other boundaries (viz., the gradients of the concentration in the direction normal to the boundary are assumed to vanish identically).

The number of grid nodes and the spatial resolution (based on wall units) used for performing DNS are summarized in table 2. The grid is uniform in the streamwise and spanwise directions. However, in order to resolve the wall shear layer, the grid spacing is gently stretched in the wall-normal direction using a hyperbolic tangent function. As shown in the table, the minimum and maximum grid resolutions in the wall-normal direction are $\Delta y^+_{min} = 0.03$ and $\Delta y^+_{max} = 4.6$ for $Re_\tau = 180$, and $\Delta y^+_{min} = 0.03$ and $\Delta y^+_{max} = 2.4$ for $Re_\tau = 395$. In general, the grid resolutions that we used for conducting DNS at the two Reynolds numbers are much finer than those used in the DNS studies of Handler *et al.* (1999) and Moser *et al.* (1999) at comparable Reynolds numbers. In their study, they used a spectral method which requires much coarser grids to resolve the turbulent scales as compared to the finite volume or finite difference methods used herein.

4 Results

In this section, the DNS results of the eight test cases are analyzed, which include the first and second moments of the velocity fluctuations, the mean and variance of the concentration field of the single and total plumes, cross correlation coefficient of the two plumes, and co-spectrum and coherency spectrum of the two concentration fields. All velocity and concentration statistics were extracted from the instantaneous velocity and concentration fields obtained from the DNS. As an example, figure 2 shows instantaneous snapshots of the velocity and concentration fields in a horizontal plane for case 4.

4.1 Velocity Statistics

The focus of this research is on the interference of two instantaneous passive plumes. However, because the dispersion of passive plumes is dominated by flow convection, it is important to examine the quality of the predicted velocity field prior to the analysis of the concentration field. Figure 3 validates the present DNS predictions for the first- and second-order velocity statistics against some available DNS data published in the literature. Our DNS results for an open-channel flow at $Re_\tau = 180$ are compared against the open-channel DNS data of Handler *et al.* (1999). However, due to a lack of numerical and experimental data for an open-channel flow at $Re_\tau = 395$, the DNS results of Moser *et al.* (1999) for a plane-channel flow (of the same Reynolds number) are used in our comparative study. For the purpose of comparison, it should be noted that the upper boundary of the open channel coincides with the central plane (at the half-channel height) of the plane channel. All velocity statistics shown in Figure 3 have been non-dimensionalized using the wall friction velocity u_τ.

Figures 3(a) and (b) show the vertical profiles of the non-dimensionalized mean streamwise velocity $U^+ \equiv U/u_\tau$ for $Re_\tau = 180$ and 395, respectively. In addition to the DNS data of Handler *et al.* (1999) and Moser *et al.* (1999), our current DNS results for the mean streamwise velocity profiles are also compared against the classical law of the wall based on von Kármán's two-layer turbulent boundary-layer model. As shown in figures 3(a) and (b), the current DNS results are in very good conformance with the reported data, exhibiting the expected mean streamwise velocity profile characteristics for a wall-shear flow.

Figures 3(c) and (d) show the vertical profiles of the three components of the non-dimensionalized root-mean-square (RMS) velocities (i.e., u_{rms}/u_τ, v_{rms}/u_τ, and w_{rms}/u_τ)

for the two Reynolds numbers tested. For the lower Reynolds number case ($Re_\tau = 180$), the RMS velocities predicted by the current simulation are in excellent agreement with the DNS results of Handler *et al.* (1999). As shown in figure 3(c), for the case of $Re_\tau = 395$, the current simulation has well predicted the three RMS velocity components in the near-wall region and throughout most of the channel below the free surface (upper boundary) in comparison with the reported DNS results of Moser *et al.* (1999) on a plane-channel flow. However, close to the upper boundary, there are some discrepancies between our current and the reported DNS results, especially as it pertains to the prediction of the wall-normal component v_{rms}/u_τ. The value of v_{rms}/u_τ for the current open channel approaches zero at the upper boundary, while that of the plane channel reaches a nonzero value. These discrepancies are expected, as they reflect the differences between the current open-channel flow case and the plane-channel flow case of Moser *et al.* (1999). In an open channel, the flow boundary condition is prescribed as being free slip (and therefore, non-penetrative in the wall-normal direction) along the free surface; however, this restriction does not hold along the central plane (at the half-channel height) in a plane-channel flow.

Figures 3(e) and (f) compare the predicted vertical profiles of the non-dimensionalized Reynolds shear stress $-\overline{u'v'}/u_\tau^2$ with the reported DNS data for $Re_\tau = 180$ and 395, respectively. As is clearly shown in both these figures, the agreement between the current and previously reported DNS data sets is excellent, and the effects of wall anisotropy on the Reynolds shear stress profile is evident at both Reynolds numbers.

4.2 Mean Concentration

With reference to the streamwise development of a single plume, three regimes can be identified using the relative width (size) of the instantaneous plume; namely, (1) the molecular diffusive range where the width of the instantaneous plume is smaller than the Kolmogorov microscale, (2) the turbulent convective range where the width of the instantaneous plume is smaller than the size of the most energetic turbulent eddies, and (3) the turbulent diffusive range where the instantaneous plume width is of the same order or larger than the size of the most energetic turbulent eddies. Figure 4 shows a schematic of these three regimes of plume development. In the molecular diffusive range, the molecular diffusion is the dominant mechanism in the plume dispersion. Because the grid resolution for our current DNS is of same order as the Kolmogorov microscale, it is not possible to simulate computation-

ally the molecular diffusive regime of plume development (which requires a study of the detailed physics of the flow and dispersion at scales finer than the Kolmogorov microscale). In the turbulent convective range, the width of the instantaneous plume is relatively small in comparison with the size of the most energetic turbulent eddies. Eddies that are smaller in size than the instantaneous plume contribute to internal development of the plume, associated with relative dispersion and internal fluctuations. In contrast, eddies with sizes that are greater than the instantaneous width of the plume contribute to the bulk meandering of the plume, associated with external fluctuations of the passive scalar. In the turbulent convective regime of plume development, the bulk meandering of the instantaneous plume provides the primary contribution to scalar fluctuations. However, its effect decreases as the downstream distance from the source increases. This is because as the downwind fetch from the concentrated (point) source increases, the instantaneous plume width increases relative to the size of the most energetic turbulent eddies. In the far downstream region of the source, the instantaneous plume width becomes comparable to and eventually larger than the size of the most energetic turbulent eddies. The development of the instantaneous plume then transitions into the turbulent diffusive regime where the major contribution to the scalar fluctuations arises from the internal fluctuations (in-plume mixing processes) and the effects of plume meander are minimal or zero.

The turbulent diffusive range of the plume development in the region far downstream of the source can be precisely identified using spectra of the velocity field. The spectrum of the spanwise velocity fluctuations is defined as

$$E_{w'w'}(k_z) = \frac{1}{2\pi}\int_{-\infty}^{\infty} e^{-ik_z\tau} R_{w'w'}(\tau) d\tau, \tag{5}$$

where k_z is the wavenumber and $R_{w'w'}(\tau)$ is the autocorrelation function of the spanwise velocity fluctuations at spatial lag τ defined as

$$R_{w'w'}(\tau) = \frac{\overline{w'(z)w'(z+\tau)}}{w_{rms}^2}. \tag{6}$$

Figure 5(a) shows the velocity spectra $E_{w'w'}(k_z)$ plotted against the wavenumber k_z for the two Reynolds number flows. The velocity fluctuations used for the computation of these spectra were obtained at the source height $y_s^+ = 5$. In order to clearly show the size of the most energetic eddies, it is more convenient to display the velocity spectra pre-multiplied by the wavenumber (i.e., $k_z E_{w'w'}(k_z)$) plotted against the normalized spanwise wavelength $\lambda_z/\delta \equiv$

$2\pi\Big/(k_z\delta)$. The wavelength corresponding to the spectral peak in this figure is associated with the size of the most energetic turbulent eddies (i.e., $\lambda_{z,m}$) of the flow, and its value is $\lambda_{z,m}/\delta = 0.597$ and 0.283 for $Re_\tau = 180$ and 395, respectively. The turbulent diffusive range can be identified (approximately or better) using the criterion that the turbulent diffusive range corresponds to that range of downwind fetches where the width of the instantaneous plume exceeds the 'size' of the most energetic turbulent eddies [1] (viz., where $2\Sigma_r \geq \lambda_{z,m}$). Here, Σ_r is the half width of the instantaneous plume in the spanwise direction and is defined as the plume spread over which the instantaneous concentration decreases to about 1% of its maximum value. To understand these concepts better, we can use the example of a Gaussian distribution. If the assumed profile of the instantaneous plume is Gaussian [2], then $2\Sigma_r = 2 \times 3\sigma_r = 6\sigma_r \geq \lambda_{z,m}$. For the two Reynolds numbers tested, the wavelengths correspond to $\sigma_r/\delta \geq 0.1$ and 0.047 (equivalently, $\sigma_z/\delta \geq 0.111$ and 0.052) for $Re_\tau = 180$ and 395, respectively. Here, σ_z and σ_r represent the mean and relative plume dispersion, respectively.

The mean plume dispersion $\sigma_z(x)$ (of a single plume) in the lateral direction at source height y_s is defined as

$$\sigma_z^2(x) = \frac{\int (z-\beta)^2 C(x, y_s, z) dz}{\int C(x, y_s, z) dz}, \tag{7}$$

where C is the mean concentration, and β is the spanwise location of the mean centroid of the plume within the plane (parallel to the bottom plate) at the source height, defined as

$$\beta(x, y_s) = \frac{\int z C(x, y_s, z) dz}{\int C(x, y_s, z) dz}. \tag{8}$$

The relative dispersion with respect to the centroid of the instantaneous plume (that is associated with internal fluctuations within the plume), and the dispersion of the centroid of instantaneous plume itself (that is associated with the bulk meandering of the plume) are the two physical mechanisms that are responsible for the growth of the mean plume. The mean plume dispersion σ_z, the relative plume dispersion σ_r and the dispersion of the centroid of instantaneous plume σ_c are related by

$$\sigma_z^2 = \sigma_r^2 + \sigma_c^2. \tag{9}$$

[1] The beginning of the turbulent diffusive range occurs when the instantaneous plume width is comparable to the size of the most energetic eddies in the flow.

[2] This is reasonable assumption at downstream locations close to the source (Warhaft, 1984).

Figure 6 shows a schematic of mean and relative dispersion for a single plume release case. In this figure, $c_r(t,z)$ and $C_r(z)$ represent the instantaneous and mean concentration in the relative frame and $z_c(t)$ is the centroid of the instantaneous plume. The value of σ_c can be calculated using a given time series of $z_c(t)$. Once the values of σ_z and σ_c are available, σ_r can be evaluated using equation 9. The streamwise variation of the non-dimensionalized lateral mean plume dispersion (σ_z/δ) and the meandering ratio (defined as $M = \sigma_c^2/\sigma_r^2$) at source height is shown in figures 7(a) and (b), respectively. Figure 7(a) shows that the mean plume dispersion for $Re_\tau = 180$ is larger than that for $Re_\tau = 395$ at a given downstream location. This is because the streamwise convection is stronger at a higher Reynolds number, and therefore, the plume has less time to spread over the same downstream distance. Figure 7(b) shows the Reynolds number effect on the meandering ratio. As the Reynolds number increases from 180 to 395, the value of M decreases at a given location downstream of the point source. This indicates that the effect of meandering decreases and that of the relative dispersion increases as the mean streamwise velocity increases. Furthermore, as shown in figure 7(b), the value of the meandering ratio decreases rapidly as the downstream distance increases. This is because the plume size near the source is much smaller than the size of the energetic eddies in the near-source region, and in this regime of plume development, the bulk flapping of the plume provides the dominant contribution to the plume concentration fluctuations. As the downstream distance from the source increases, the plume grows in size, the meandering effect reduces and the mechanism of relative dispersion becomes more and more prominent.

In figures 7(a) and (b), the downstream positions where the width of the instantaneous plume reaches the size of the most energetic turbulent eddies are indicated using a dash and dash-dot-dotted lines for $Re_\tau = 180$ and 395, respectively. Downstream of these positions, the plume is in the turbulent diffusive range, whereas, upstream of these positions, the plume is either in the turbulent convective range or in transition to the turbulent diffusive range. Apparently, both ranges of plume diffusion have been well captured by the simulation at the two Reynolds numbers. As shown in the figure, the beginning of the turbulent diffusive regimes occur at $x/\delta = 1.5$ and 0.6 for $Re_\tau = 180$ and 395, respectively.

As can be seen in figure 7, the instantaneous plume width for the lower Reynolds number flow reaches the size of the most energetic eddies in the flow at a greater downwind distance from the source than that for the higher Reynolds number flow. As shown previously in

figure 5, this is due to the fact that the size of the most energetic eddies is larger for $Re_\tau = 180$ than that for $Re_\tau = 395$. This also causes the meandering ratio M for $Re_\tau = 180$ to be larger than that for $Re_\tau = 395$ as is shown in figure 7(b). Figure 7(b) also shows that when the width of the instantaneous plume reaches the size of the most energetic turbulent eddies, the meandering ratio is approximately equal to 0.25 for both Reynolds numbers (i.e. $M = 0.25$, as indicated using a horizontal solid line).

The scalar transport equation represented by equation 3 is linear with respect to the instantaneous concentration c field. Therefore, the mean concentration fields generated by the two point sources are linearly superposable and the total mean concentration can be simply determined as $C_T = C_A + C_B$. The mean concentration profiles of the single and total plumes for cases 3 and 7 are shown in figure 8 at three downstream locations corresponding to $x/\delta = 1$, 3 and 6. In this figure, the mean concentration has been non-dimensionalized using the concentration level at the source C_s. As shown in figures 8(a) and (b), close to the source, the total mean concentration profiles exhibit a dual-peak pattern, and the lateral positions of the two peaks coincide with the lateral positions of the two sources located at $z/\delta = 1.95$ and 2.25 for $Re_\tau = 180$ and at $z/\delta = 1.43$ and 1.71 for $Re_\tau = 395$, respectively. However, as the downwind distance from the sources increases, the distinct dual-peak pattern in the total mean concentration evident at the near-source locations disappears. As is clear in figures 8(c)-(f), the lateral profile of the total plume (as the linear superposition of the mean concentration from the two single plumes) transitions to a single-peak pattern. This transition is due to the fact that in the far downstream regions at $x/\delta = 3$ and 6, the two single plumes spread significantly in the lateral direction, such that the peak value of each single plume begins to merge with each other. Due to the equal strength of the two sources, the profile of the total concentration always shows a perfect symmetry in the lateral direction. By comparing figures 8(c) with 8(d) and 8(e) with 8(f), it is clear that the transition from the dual-peak to single-peak pattern in the total mean concentration profile occurs earlier in case 3 than in case 7. This physical feature is expected, and is consistent with the previous analysis of the single plume in figure 7(a) which indicates that the single plume width is wider in the lateral direction at the lower Reynolds number (case 3) than at the higher Reynolds number (case 7). As such, the peak value of the single plume is smaller at the lower Reynolds number, which facilitates the transition from the dual-peak to the single-peak pattern in the

total mean plume.

Figure 9 shows the mean concentration profiles of the total plume for cases 3 and 7 at $x/\delta = 6$ for six values of y^+. In general, the profiles of the mean total plume exhibit Gaussian patterns at these 6 elevated positions relatively far downstream of the sources. It is seen that as the vertical distance above the source increases, the mean concentration level decreases monotonically. By comparing figures 9(a) and (b), it is clear that for a fixed y^+ value, the mean concentration level of case 3 ($Re_\tau = 180$) is higher than that of case 7 ($Re_\tau = 395$). This feature is expected. As the Reynolds number increases, the streamwise convection becomes stronger and the total plume is less spread in the vertical direction.

4.3 Variance of Concentration Fluctuations

In the previous subsection, we have demonstrated that first-order concentration statistics of two plumes are linearly superposable. However, the second-order concentration statistics of two plumes are not linearly superposable. Specifically, it is known that $\overline{c_T'^2} \neq \overline{c_A'^2} + \overline{c_B'^2}$ holds generally, which arises from the nonlinear characteristics (in terms of second- and higher-order concentration statistics) of dual-plume interference. Figures 10(a) and (b) show the lateral profiles of the sum of the variances of concentration fluctuations of each single plume (i.e., $\overline{c_A'^2} + \overline{c_B'^2}$) and the variance of concentration fluctuations of the total plume (i.e., $\overline{c_T'^2}$) at $x/\delta = 4$ for cases 3 and 7, respectively. The ordinate of this figure is non-dimensionalized by the maximum variance of the concentration fluctuations for the total plume ($\overline{c_{T,m}'^2}$). As is evident from the figure, the sum of the variances is not equal to the variance of the total plume in general. For cases 3 and 7, within the central lateral region between the two sources, the sum of the variances is larger than the variance of the total plume; whereas, in the immediate lateral region of the two sources, the sum of the variances is smaller than the variance of the total plume. Furthermore, only in the far lateral regions of the sources does the sum of the variances equal the variance of the total plume.

The above observations can be precisely explained using the following identity

$$\overline{c_T'^2} = \overline{(c_A' + c_B')^2} = \overline{c_A'^2} + \overline{c_B'^2} + 2\overline{c_A' c_B'}, \tag{10}$$

where c_A' and c_B' are the fluctuating components of the instantaneous concentration for the plumes released from sources A and B, respectively, and $\overline{c_A' c_B'}$ is the covariance of the concentration fluctuations of the two plumes. Equation 10 indicates that the variance of

concentration fluctuations of the total plume produced by the two point sources is not linearly superposable, because an additional term relating to the covariance of two single plumes needs also to be included. In the far lateral region, because the covariance between the two plumes decreases significantly ($\overline{c'_A c'_B} \to 0$), the variances of concentration fluctuations of two plumes become approximately superposable. In the remainder of the paper, the relationship between the mean (C_T) and the variance ($\overline{c'^2_T}$) of the total plume is examined, and the property of the covariance of the concentration fluctuations of two instantaneous plumes will be further examined using the cross correlation coefficient, concentration co-spectrum and coherency spectrum.

Through the previous analysis, it has been shown that the turbulent diffusive range in the streamwise plume development starts at $x/\delta = 1.5$ and 0.6 for $Re_\tau = 180$ and 395, respectively. Within the turbulent diffusive range, the external plume fluctuations (e.g., meandering effect) is small in comparison with that of the internal plume fluctuations (e.g., relative dispersion and in-plume mixing). The production term in the transport equation for the variance of concentration fluctuations is proportional to the mean concentration gradient, i.e. $Pr = -2\overline{u'_i c'} \cdot \frac{\partial C}{\partial x_i} \propto \frac{\partial C}{\partial x_i}$ (see, e.g. Wang *et al.* (2009)). Therefore, as a necessary condition, locations where the mean concentration gradient is zero (corresponding to the local extrema of the mean concentration profile) can be also potentially the locations for the local minima of the variance (since these locations correspond to locations of minimum variance production rate). On the other hand, because the production term functions as a source for the concentration variance, a large absolute value in the local mean concentration gradient tends to increase the local production rate, which in turn leads to an increase in the value of concentration variance. As such, locations where the absolute mean concentration gradient is maximum can be also potentially the locations for the local maxima of the concentration variance. Figure 11 compares the lateral profiles of the mean (C_T) and variance ($\overline{c'^2_T}$) of the total plume at the source height ($y_s^+ = 5$) for cases 3 and 7 at three downstream locations. All profiles have been non-dimensionalized using their maximum values. As expected, at all downstream locations, the extrema locations in the C_T profile coincide with the locations associated with the local minima in $\overline{c'^2_T}$, and the locations of the maximum absolute gradient of C_T coincide with the locations of the local maxima in $\overline{c'^2_T}$. Similar behavior is also observed for the other test cases at the source height. This relationship between the mean and the

variance of the concentration is also observed and investigated by Karnik and Tavoularis (1989) for a single plume dispersion in a uniformly sheared, nearly homogeneous turbulent flow. They found that at locations far downstream of the source, where the ratio of the streamwise velocity lengthscale to the half-width of the mean plume (which measures the strength of the plume meandering) is small, local conditions prevail and the concentration variance is nearly proportional to the local value of the mean concentration gradient. This is consistent with the above discussion and the results shown in figure 11 for the total plume.

The phenomenon of the appearance, disappearance and subsequent reappearance of the off-axis peaks in the concentration variance profiles with respect to the downstream location from the source is well established in the literature for single-source (Stapountzis *et al.*, 1986; Karnik and Tavoularis, 1989) and dual-source dispersion (Warhaft, 1984; Costa-Patry and Mydlarski, 2008) problems. In order to provide a better insight into this phenomenon, the effect of the wall distance on the concentration variance profile is studied in the remainder of this section. Figure 12 shows the spanwise profiles of the non-dimensionalized variance of concentration fluctuations of the total plume for cases 3 and 7 at $x/\delta = 6$ for different values of y^+. As is clear from figure 12(a), the spanwise profile of $\overline{c_T'^2}/\overline{c_{T,m}'^2}$ exhibits a distinct dual-peak pattern at lower elevations for $5 \leq y^+ \leq 15$. As the vertical distance from the wall increases, the dual-peak pattern vanishes around $y^+ = 50$ but reappears as the value of y^+ continues to increase (for $y^+ \geq 80$). By comparing figures 12(a) and (b), it is clear that this interesting dual-single-dual-peak pattern transition with increasing elevation is common to both case 3 (for $Re_\tau = 180$) and case 7 (for $Re_\tau = 395$), albeit these pattern transitions occur at higher y^+ values in case 7 than in case 3.

It is interesting to note that the current observation of the dual-single-dual-peak transitions in the concentration variance profiles with increasing wall-normal distance from the bottom boundary at a fixed downstream distance is analogous to that described by Stapountzis *et al.* (1986) and Karnik and Tavoularis (1989) with respect to the downstream distance from the source at a fixed wall-normal distance. A similar interpretation can be used to explain the dual-single-dual-peak transitions with increasing height above the bottom wall at a fixed downstream location. Stapountzis *et al.* (1986) and Karnik and Tavoularis (1989) attributed the phenomenon of dual-single-dual-peak pattern transitions in the evolution of concentration variance profiles with increasing downstream distance from the source

to the degree of meandering motions in the plume. These researchers further indicated that the dual-single-peak transition near the source is caused by the enhanced meandering as the downstream distance from the source increases, and meandering is a major source of concentration fluctuations in the region near the source. As the plume grows further in width (relative to the integral scales of turbulence), the effects of the meandering diminish and the single-dual-peak transition in the concentration variance profiles occurs at further downstream distances from the source.

For a given downstream location from the source, as the vertical distance from the wall increases, the size of the most energetic eddies of turbulence increases, and consequently, the meandering effect enhances and becomes the dominant source of concentration fluctuations. Then, the concentration fluctuations can be transported to locations of maximum absolute mean concentration gradients by turbulent eddies from the regions with zero or small mean concentration gradients, or vice versa. This mechanism "smears out" the local maxima and minima of the variance, leading to a single-peak pattern in the concentration variance profile. This explains the first transition from a dual- to a single-peak pattern profile, occurring within the range $30 < y^+ \leq 50$ for $Re_\tau = 180$ (case 3) and within the range $50 < y^+ \leq 80$ for $Re_\tau = 395$ (case 7). The second transition from a single- to a dual-peak pattern profile takes place at a higher elevation close to the free surface (located at $y^+ = 180$ and 395 for cases 3 and 7, respectively) of the open channel. As the free surface is approached, the upward-downwind distance from the point sources increases significantly, and both concentration and concentration variance levels drop significantly. These factors further lead to reduction in meandering effects and reemergence of the dual-peak pattern in the lateral profiles of the total concentration variance.

4.4 Cross Correlation Coefficient

The non-dimensionalized form of the scalar covariance $\overline{c'_A c'_B}$ represents a cross correlation of the two plumes, defined as

$$\rho_{cc} \equiv \frac{\overline{c'_A c'_B}}{(\overline{c'^2_A}\,\overline{c'^2_B})^{1/2}} = \frac{\overline{c'^2_T} - \overline{c'^2_A} - \overline{c'^2_B}}{2(\overline{c'^2_A}\,\overline{c'^2_B})^{1/2}}. \tag{11}$$

Equivalently, ρ_{cc} can be expressed as

$$\rho_{cc} = \frac{\overline{c_A c_B} - C_A C_B}{(\overline{c'^2_A}\,\overline{c'^2_B})^{1/2}}. \tag{12}$$

According to Costa-Patry and Mydlarski (2008), the cross correlation ρ_{cc} reflects the quality of mixing while the scalar covariance reflects the total amount of mixing.

The streamwise variation of the cross correlation at the midpoint between the two plumes at the source height for cases 1-8 is shown using linear and semi-logarithmic scales in figures 13(a) and (b), respectively. The Reynolds number effects on the value of ρ_{cc} can be ascertained if we compare cases with a similar source separation distance (but different Reynolds numbers). By comparing cases 1 with 5, 2 with 6, 3 with 7, and 4 with 8, it becomes clear that the effect of Reynolds number on the streamwise variation of ρ_{cc} is insignificant (at least over the limited Reynolds number range for which we have data). Meanwhile, it is evident that the source separation distance has a significant impact on the streamwise distribution of ρ_{cc}. Following the lead of Warhaft (1984) and Costa-Patry and Mydlarski (2008), the streamwise evolution of ρ_{cc} at the midspan between the two plumes can be generally categorized into the following four stages of development:

(1) First stage (zero interference, $\rho_{cc} \approx 0$)

Very close to the source, there is no interaction between the two plumes. In other words, the width of the mean plume $2\Sigma_z$ and the width of the instantaneous plume $2\Sigma_r$ are smaller than the source separation distance d (i.e., $2\Sigma_z < d$ and $2\Sigma_r < d$) and the location at the midpoint between the two plumes is never exposed to both plumes simultaneously with the consequence that $\overline{c_A c_B} = 0$ and $C_A C_B = 0$. As a result, ρ_{cc} is identically zero in the region immediately downstream of the source. As shown in figures 13(b), this conclusion holds strictly for cases 4 and 8, whose source separation distances are the largest among all the test cases. The downstream extent of this stage reduces as the source separation distance d decreases. As such, for cases with smaller source separation distances (i.e., for cases 1, 2, 5 and 7), this stage (with $\rho_{cc} \approx 0$) cannot be observed as the mean plumes overlap almost immediately after the scalar is released from the two sources.

(2) Second stage (destructive interference, $\rho_{cc} < 0$)

As the downstream distance from the sources increases, the widths of the mean and instantaneous single plume exceed[3] the source separation distance d. In this stage,

[3] The width of the mean plume exceeds the source separation distance at a smaller downstream

$\overline{c_A c_B} < C_A C_B$ and therefore, ρ_{cc} is negatively valued (cf. equation 12). The physical mechanism can be explained as follows. In the second stage and for small meandering motions, a relatively large eddy can transport a concentration "patch" from one plume to the other, causing the concentration to decrease in one plume while simultaneously increasing it in the other. However, for strong meandering motions, Warhaft (1984) and Costa-Patry and Mydlarski (2008) attributed the negative cross correlation to the physical mechanism whereby a large eddy can move one plume off the measurement location while simultaneously moving the other plume onto the location. In both scenarios, the cross correlation value ρ_{cc} is negative at the measurement location.

From figure 13, it is observed that ρ_{cc} reaches its minimum value (a negatively valued trough) during this stage, and then increases towards a positive value with increasing distance from the source. Furthermore, it is clear that the smaller the source separation distance is, the shorter is the streamwise extent of this stage and the larger (in absolute magnitude) is the negative cross correlation between the two plumes. Following Costa-Patry and Mydlarski (2008), the region where $\partial\rho_{cc}/\partial x < 0$ is typically characterized by the sampling of one plume or the other but not both. As the size of the instantaneous plumes increases, the measurement location is exposed to both plumes for a longer time and $\partial\rho_{cc}/\partial x$ becomes positive. Based on this, it is understood that the region in which $\partial\rho_{cc}/\partial x < 0$ holds corresponds to the downstream locations where only the width of the mean plume exceeds the source separation distance d while the width of the instantaneous plume is still smaller than d. Due to the small meandering motions for the cases considered in this study, the width of the instantaneous plume is only slightly smaller than that of the mean plume. Therefore, the downstream region which features $\partial\rho_{cc}/\partial x < 0$ is much shorter here than that observed in Costa-Patry and Mydlarski (2008) which involved larger meandering motions due to the higher source elevations above the bottom wall. Indeed, as shown in figure 13, for cases 1 and 5 (for which the source separation is the smallest), the negatively valued trough of ρ_{cc} is the sharpest and the largest (in absolute magnitude), resulting in the shortest destructive interference range among all the test cases.

location than does the instantaneous plume, because the mean plume width is always larger than or equal to the instantaneous plume width.

(3) Third stage (constructive interference, $\rho_{cc} \geq 0$)

It is well-known (see, e.g. Costa-Patry and Mydlarski (2008)) that meandering of the plume and internal turbulent mixing are the two mechanisms that cause $\overline{c_A c_B} \geq C_A C_B$ (or equivalently, $\rho_{cc} \geq 0$). However, from the previous analysis, it has been demonstrated that plume meandering effects are negligible over the downstream region for $x/\delta > 1.5$ and 0.6 at $Re_\tau = 180$ and 395, respectively. The third stage in the development of the cross correlation of all test cases occurs in this downstream region of the source. Therefore, the cross correlation in this stage of development mainly arises from the internal turbulent mixing of the two plumes which depends on a complicated physical process involving the stretching and folding of contaminant elements along with turbulent motions. When a blob of tracer is injected into a turbulent flow, it quickly deforms into thin folded strands and sheets. Turbulent fluid motions that repeatedly stretch and fold the contaminant elements serve also to increase the contact area for inter-diffusion and, hence, to enhance the molecular mixing, and to homogenize the plume concentration as the large spatial concentration gradients that are generated by the turbulent stirring are rapidly smeared out by molecular diffusion (Yee *et al.*, 2003). This micromixing of the scalars from the two plumes makes a dominant contribution to the constructive interference of the two plumes in this stage. Specifically, $\overline{c_A c_B} \geq C_A C_B$ holds, and therefore, according to equation 12, the cross correlation is positive (i.e., $\rho_{cc} \geq 0$). Furthermore, as the source separation distance decreases, the correlation between the two instantaneous plumes ($\overline{c_A c_B}$) in this stage of development increases drastically, leading to a fast growth in the value of ρ_{cc} with increasing downwind distance. As shown in figures 13, this trend in the streamwise development of ρ_{cc} is the most strongly expressed for cases 1 and 5 (the source separation distances are the smallest among all test cases, see Table 1). However, for cases with larger source separation distances (such as cases 3, 4, 7 and 8), the increase in ρ_{cc} towards unity cannot be fully captured owing to the limited downwind extent in our current simulations.

(4) Fourth stage (complete mixing, $\rho_{cc} \approx 1$)

In this final stage of development, the source separation distance is negligible in comparison with the long downstream distance from the sources. As such, the two plumes are completely mixed (i.e., $\rho_{cc} \to 1$) and the total plume behaves as if it comes

from a single source. A comparison of the profiles exhibited in figures 13 indicates that the cases with a smaller source separation distance tend to reach this complete mixing state earlier than the cases with a larger source separation distance. Such an asymptotic behavior is captured in cases 1 and 5, and partially captured in cases 2 and 6. However, in order to reproduce this complete mixing stage in cases 3, 4, 7 and 8, a much longer downwind fetch would be required in the simulations.

It is seen that ρ_{cc} at source height is only a function of source separation distance d and the measurement locations. This is similar to the observation of Warhaft (1984) in grid turbulence. Generally, ρ_{cc} reaches the complete mixing state faster in this study than in the case of grid turbulence of Warhaft (1984). This can be attributed to the highly-sheared region near the wall (associated as such with hairpin structures and streak structures, etc.) where small-scale eddies are generated to increase the internal mixing in the plume. In addition to this, Costa-Patry and Mydlarski (2008) noted that by limiting both the growth and meandering of the plume while simultaneously increasing the turbulence kinetic energy, the presence of the wall will lead necessarily to an increased internal plume mixing.

Figures 14(a)-(c) compare the lateral profiles of ρ_{cc} for the 8 different cases at the source height for three different downwind distances. The Reynolds number effects on the lateral profile of ρ_{cc} are also directly compared in this figure. Owing to the relatively long streamwise domain size used in cases 1-4 (for $Re_\tau = 180$), the influence of the source separation d on the profile of ρ_{cc} is singled out in the fully turbulent diffusive range (for $x/\delta = 12$), and the results are displayed in figure 14(d). To further facilitate our comparative study, the lateral coordinate has been shifted to the midpoint location between the two plumes (z_{mid}) and then non-dimensionalized using the mean plume dispersion. Consistent with our previous analysis of the streamwise profiles of ρ_{cc} given in figure 13, figure 14 also shows clearly that the dominant factor that determines the shape of the lateral profile of ρ_{cc} is the source separation distance d. By comparing cases 1 with 5, 2 with 6, 3 with 7, and 4 with 8, the effect of Reynolds number on the lateral profiles of ρ_{cc} can be observed, which appears to be much smaller than that of the source separation distance d.

The streamwise variation in the shape of the lateral profiles of ρ_{cc} also illustrates the four stages in its evolution. In the first stage, the shape of the profile is flat with a zero value, because there is no interaction between the two plumes. In the second stage, a M-

shaped profile, with a negative minimum value, begins to form. The M-shaped profile has the minimum value of ρ_{cc} located midway between the two plumes and the maximum values are found at the edges of the plumes. As discussed earlier, the minimum value at the midpoint between the two plumes is due to the fact that a large eddy (relative to the plume width) at this location can cause the concentration contributed by one plume to increase and that contributed by the other plume to decrease. For sources that are close enough together, the maximum values in ρ_{cc} on both sides of the centerline (where the plume intermittency is large) arise from the fact that at these locations a large eddy can occasionally transport both plumes (in case of strong meandering) or bring together a patch of concentration from each of the plumes (in case of weak meandering), causing the two concentrations to either increase or decrease simultaneously. A similar M-shaped profile of ρ_{cc} was also observed by Warhaft (1984) in grid turbulence, Tong and Warhaft (1995) in a turbulent jet and Costa-Patry and Mydlarski (2008) in a turbulent plane-channel flow. Due to the noise sensitivity of their measurements, these investigators were unable to demonstrate conclusively that the value of ρ_{cc} approaches zero at the extreme lateral fringes of the plume. However, this is clearly demonstrated in figure 14. At the third stage in the development, the minimum of the M-shaped profile becomes positive and the profile begins to approach a constant value of unity (approximately or better), owing to the internal turbulent mixing of the two plumes. Finally at the fourth stage of development, a flat profile with a value of unity forms signaling that the scalars in the two overlapping plumes are perfectly well mixed.

4.5 Concentration Co-spectrum and Coherency Spectrum

The quantities studied so far contain no information about the scales of mixing of the two plumes. However, mixing of the two plumes is a multi-scale phenomenon, as the turbulent motions responsible for stirring act primarily on large and intermediate scales, with the molecular diffusion smearing out and completing the mixing at the smallest scales. Therefore, in order to improve our understanding of the physics of mixing of two plumes, the scales of the concentration fields that contribute to the turbulent stirring and molecular mixing need to be investigated. The information about the scales of mixing can be quantified using the so-called co-spectrum and coherency spectrum of the two plumes. Following the approach of Tong and Warhaft (1995) and Costa-Patry and Mydlarski (2008), the co-spectrum is defined

as

$$Co_{c'_A c'_B}(f) = \left(E_{c'_T c'_T}(f) - E_{c'_A c'_A}(f) - E_{c'_B c'_B}(f)\right)/2, \tag{13}$$

where $E_{c'_A c'_A}(f)$, $E_{c'_B c'_B}(f)$ and $E_{c'_T c'_T}(f)$ are the concentration power spectra for plume A, plume B, and the total plume, respectively. The integral of the non-dimensionalized co-spectrum ($Co_{c'_A c'_B}(f)/(\overline{c'^2_A}\,\overline{c'^2_B})^{1/2}$) is the cross correlation coefficient ρ_{cc}, i.e.

$$\rho_{cc} = \int_{-\infty}^{\infty} Co_{c'_A c'_B}(f)/(\overline{c'^2_A}\,\overline{c'^2_B})^{1/2} df. \tag{14}$$

The coherency spectrum ρ_{cs} is defined as

$$\rho_{cs}(f) = \frac{Co_{c'_A c'_B}(f)}{\left(E_{c'_A c'_A}(f) E_{c'_B c'_B}(f)\right)^{1/2}}, \tag{15}$$

which describes the cross correlation coefficient in the frequency space. The pre-multiplied co-spectrum and the coherency spectrum obtained at the midpoint between the two plumes at source height for cases 1 and 5 are shown in figures 15 and 16, respectively. In order to investigate the streamwise evolutions of the pre-multiplied co-spectrum and coherency spectrum, several downstream locations (with different x/δ values) are considered in our comparative study. The frequency in these figures has been non-dimensionalized using u_τ and δ, which leads to the Strouhal number defined as $f^* = f\delta/u_\tau$. In order to facilitate the discussion, the frequency corresponding to the Kolmogorov scale of the velocity field is shown using a straight vertical dashed line in figure 16. Furthermore, in order to identify the most energetic eddy scale and compare the local plume scale with it, the pre-multiplied energy spectrum of the spanwise velocity fluctuations (i.e., $f^* E_{w'w'}(f^*)$) is plotted using a long dashed curve in figure 16.

By definition, the co-spectrum $Co_{c'_A c'_B}(f)$ and coherency spectrum $\rho_{cs}(f)$ studied here are closely related to the cross correlation coefficient ρ_{cc}, with a difference that $Co_{c'_A c'_B}(f)$ and $\rho_{cs}(f)$ provide explicit information on the interference of the two plumes in the frequency space, whereas ρ_{cc} provides similar information in physical space. As such, it is useful to connect the physical features shown in figures 15 and 16 (in the frequency space) to those shown in figures 13 and 14 (in the physical space). Here, we only present $Co_{c'_A c'_B}(f)$ and $\rho_{cs}(f)$ for cases 1 and 5, because these two cases (as shown previously in figure 13) cover the widest range of values for ρ_{cc} among all the test cases. Also, except for the first stage, all other three stages in the development of the cross correlation are well captured by these two cases.

The values for $Co_{c'_A c'_B}(f)$ and $\rho_{cs}(f)$ in the first stage can be determined as $Co_{c'_A c'_B}(f) = 0$ and $\rho_{cs}(f) = 0$, simply because there is no interference between the two plumes.

As shown previously in figures 13 and 14, the streamwise variation of the cross correlation is less sensitive to the Reynolds number than the source separation distance. A similar conclusion can be made for the streamwise variation of the pre-multiplied co-spectrum and the coherency spectrum by comparing figures 15(a) with 15(b) and 16(a) with 16(b). Furthermore, the streamwise evolution of the pre-multiplied co-spectrum and the coherency spectrum follows the streamwise evolution of the cross correlation and the aforementioned four stages in the development for the cross correlation can also be observed in the behavior of the pre-multiplied co-spectrum and coherency spectrum.

In the first stage, because the measurement location is exposed to clean fluid most of the time, it is expected that the pre-multiplied co-spectrum exhibit values near zero at all scales. This is the case for a large source separation distance and for downstream locations close to the source. In the second stage of development, the two plumes meander in opposite directions as the result of the large-scale turbulent stirring. As is explained in subsection 4.4, this produces a negative spectral peak for the pre-multiplied co-spectrum at large scales (low frequencies). The frequency of this peak can be interpreted as the frequency of the most energetic scales of the mixing of the two plumes. The value of the cross correlation is mainly determined by these scales. Because the size of the plumes increases as the downstream distance from the sources increases, the frequency of the peak decreases. Indeed, as shown in figures 15(a) and (b), the peak frequency for $x/\delta = 1$ is lower than that for $x/d = 0.5$ in cases 1 and 5.

In the third stage, the internal turbulent stirring and molecular mixing of the two plumes is expected to give rise to a positive spectral peak in the pre-multiplied co-spectrum. As the downstream distance from the sources increases, the value of this spectral peak increases and its frequency drops (indicating the scales of mixing become larger). This physical feature is evident for $x/\delta \geq 3$ in figures 15(a) and (b). In the fourth stage where the cross correlation reaches its maximum value of unity, it can be anticipated that the pre-multiplied co-spectrum reaches its asymptotic form and does not change further with increasing downstream distance from the source. Indeed, as shown in figure 15(a), as the downstream distance x/δ increases from 6 to 12, the profile of the pre-multiplied co-spectrum hardly changes.

From the above analysis, it is seen that the most energetic scales of the mixing of the two plumes, which mainly determine the cross correlation value, are generally associated with low frequencies (or, large scales). This is consistent with the observations of Tong and Warhaft (1995) and Costa-Patry and Mydlarski (2008). A physical explanation to this phenomenon is that large-scale eddies contain most of the turbulence energy, and consequently, the co-spectrum and cross correlation values are mainly determined by these large-scale eddy motions.

Figure 16 shows the streamwise variation of the coherency spectrum $\rho_{cs}(f)$, which is closely related to the cross correlation displayed in figure 13. However, it can be seen that at some small scales the coherency spectrum develops faster than at other scales. These small scales are two to ten times the Kolmogorov scale (shown using vertical dashed line in the figure) and are referred to here as the "leading scales", because the value of $\rho_{cs}(f)$ is the largest at these scales. As shown in the figure, $\rho_{cs}(f)$ at the leading scales can reach its asymptotic value of unity faster than at any other scales. A careful perusal of the figure indicates that the frequency of the leading scales is either higher than (or comparable to) the frequency of the most energetic eddies of turbulence (indicated by the peak frequency of the pre-multiplied energy spectrum $f^*E_{w'w'}(f^*)$ in the figure). This means that the rate of turbulent mixing of the two plumes becomes more efficient (faster) for those scales that are several times larger than the Kolmogorov scale and extending up to the scale of the most energetic eddies of the turbulent flow. In contrast, Tong and Warhaft (1995) and Costa-Patry and Mydlarski (2008) inferred from their analysis that the rate of mixing is fastest at the largest scales. Costa-Patry and Mydlarski (2008) attributed this to the fact that turbulence production is essentially a large-scale phenomenon, such that its effects occur first at the largest scales and these effects will be influenced by smaller scales only after a sufficient time has passed for the mixing effects to cascade down from larger to smaller scales. The reason the rate of mixing is the fastest at the largest scales in Tong and Warhaft (1995) and Costa-Patry and Mydlarski (2008) is that the plume meandering effect is dominant in these studies, which first takes place at the largest scales and subsequently is transferred down to the smaller scales. However, for the ground-level sources studied here, the plume meandering effect is negligible. Instead, the internal turbulent mixing is dominant, which first occurs at the smaller leading scales with their effects transferred subsequently to the other scales.

5 Conclusions

The interference of plumes released from two near-ground level point sources into an open-channel flow at two Reynolds numbers is studied using DNS. The first- and second-order statistics of the velocity and concentration fields have been analyzed. In order to investigate the effects of Reynolds number and source separation distance on the mixing of the two plumes, the cross correlation function, co-spectra and coherency spectra of the two concentration fields are examined. Because the transport equation for the instantaneous concentration field is linear, the mean concentration (first-order concentration moment) of the total plume can be obtained as a sum of the mean concentration of each plume. However, other concentration moments (e.g., second-order and higher) are not linearly superposable and the interference of the two plumes should be taken into account for calculations of higher-order concentration moments of the total plume.

The streamwise variation of the cross correlation function (ρ_{cc}) at the midpoint between the two plumes reveals that there are four stages in the mixing process, including (1) the zero interference stage where $\rho_{cc} \equiv 0$, (2) destructive interference stage where $\rho_{cc} < 0$, (3) constructive interference stage where $\rho_{cc} \geq 0$, and (4) complete mixing state where $\rho_{cc} \to 1$. At the source height, the streamwise evolution of the cross correlation ρ_{cc} is insensitive to the Reynolds number but highly sensitive to the source separation distance d. For a small source separation case, as the downstream distance from the sources increases, the cross correlation first decreases and then it increases towards the asymptotic value of unity. However, for a larger source separation case, the streamwise evolution of the cross correlation is slower and requires a much longer downwind fetch to approach the asymptotic state.

The results of the pre-multiplied co-spectrum ($f^* Co_{c'_A c'_B}$) and the coherency spectrum (ρ_{cs}) obtained at the midpoint between the two plumes at source height for different downstream locations can provide deeper insights into plume mixing at different scales. In the first stage (zero interference stage), because the midpoint between the two plumes is exposed to clean fluid most of the time, the pre-multiplied co-spectrum is zero at all scales. In the second stage (destructive interference stage), due to large-scale turbulent motions, patches of concentration are transported from one plume to the other, resulting in a negatively valued peak in the pre-multiplied co-spectrum at low frequencies (corresponding to large scales). In the third stage (constructive interference stage), the internal turbulent stirring and molec-

ular mixing of the two plumes give rise to a positive spectral peak in the pre-multiplied co-spectrum. As the downstream distance increases, the magnitude of this spectral peak increases monotonically as its frequency decreases (correspondingly, the scale of mixing becomes larger). In the fourth stage (complete mixing state), the cross correlation ρ_{cc} reaches its maximum value of unity, and subsequently, the pre-multiplied co-spectrum reaches its asymptotic form.

It is observed that there is a range of 'leading scales' which correspond to the largest values of ρ_{cs} in the coherency spectrum. These scales are typically two to ten times larger than the Kolmogorov scale but are smaller than or comparable to the scale of the most energetic eddies of turbulence. Within this range of leading scales, the mixing of two plumes is the fastest and ρ_{cs} approaches the asymptotic value of unity quicker than at any of the other scales.

As part of some future work, the results of the present study can be used to investigate various closure hypotheses that have been used (proposed) for dispersion modeling (e.g., the simple gradient diffusion hypothesis). In addition, the budget terms in the transport equations for the concentration flux and the concentration variance of the single and total plumes can be obtained (requiring, as such, much longer sampling times for the velocity and concentration fields than have been used in the present study in order to ensure the statistical convergence of these terms).

Acknowledgments

The authors would like to thank Western Canada Research Grid (WestGrid) for access to their supercomputing facilities. Research funding from Natural Sciences and Engineering Research Council (NSERC) of Canada to B.-C. Wang is gratefully acknowledged.

References

Boppana, V. B. L., Xie, Z.-T. and Castro, I. P. (2012). Large-eddy simulation of dispersion from line sources in a turbulent channel flow. *Flow, Turb. Combust.*, 88:311–342.

Brethouwer, G., Boersma, B. J., Pourquie, M. B. J. M. and Nieuwstadt, F. T. M. (1999). Direct numerical simulation of turbulent mixing of a passive scalar in pipe flow. *Eur. J.*

Mech. B/Fluids, 18:739–756.

Choi, H. and Moin, P. (1994). Effect of the computational time step on numerical solutions of turbulent flow. *J. Comp. Phys.*, 113:1–4.

Costa-Patry, E. and Mydlarski, L. (2008). Mixing of two thermal fields emitted from line sources in turbulent channel flow. *J. Fluid Mech.*, 609:349–375.

Davis, B. M., Jones, C. D., Manning, A. J. and Thomson, D. J. (2000). Some field experiments on the interaction of plumes from two sources. *Quart. J. Roy. Meteorol. Soc.*, 126:1343–1366.

Fackrell, J. E., Robins, A. G. (1982). The effects of source size on concentration fluctuations in plumes. *Boundary-Layer Meteorol.*, 22:335–350.

Gaskell, P. and Lau, A. (1988). Curvature-compensated convective transport: SMART, a new boundedness-preserving transport algorithm. *Int. J. Numer. Methods Fluids*, 8:617-641.

Gifford, F. (1959). Statistical properties of a fluctuating plume dispersion model. *Adv. Geophys*, 6:117-137.

Ham, F. E., Lien, F.-S. and Strong, A. B. (2002). A fully conservative second-order finite difference scheme for incompressible flow on nonuniform grids. *J. Comp. Phys.*, 177:117–133.

Handler, R. A., Saylor, J. R., Leighton, R. I. and Rovelstad, A. L. (1999). Transport of a passive scalar at a shear-free boundary in fully developed turbulent open channel flow. *Phys. Fluids.*, 11:2607–2625.

Karnik, U. and Tavoularis, S. (1989). Measurements of heat diffusion from a continuous line source in a uniformly sheared turbulent flow. *J. Fluid Mech.*, 202:233–261.

Livescu, D., Jaberi, F. A. and Madnia, C. K. (2000). Passive-scalar wake behind a line source in grid turbulence. *J. Fluid Mech.*, 416:117–149.

Moser, R. D., Kim, J. and Mansour N. N. (1999). Direct numerical simulation of turbulent channel flow up to $Re_\tau = 590$. *Phys. Fluids.*, 11:943–945.

Stapountzis, H. (1988). Covariance and mixing of temperature fluctuations from line sources in grid turbulence. *Transport Phenomena in turbulent flows. Eds. Hirata M. and Kasagi N.* Hemisphere, New York, 419–431.

Stapountzis, H., Sawford, B. L., Hunt, J. C. R. and Britter, R. E. (1986). Structure of the temperature field downwind of a line source in grid turbulence *J. Fluid Mech.*, 165:401–424.

Tong, C. and Warhaft, Z. (1995). Passive scalar dispersion and mixing in a turbulent jet. *J.*

Fluid Mech., 292:1–38.

Vrieling, A. J. and Nieuwstadt, F. T. M. (2003). Turbulent dispersion from nearby point sources–interference of the concentration statistics. *Atmos. Environ.*, 37:4493–4506.

Wang, B.-C., Yee, E. and Lien, F.-S. (2009). Numerical study of dispersing pollutant clouds in a built-up environment. *Int. J. Heat Fluid Flow*, 30:3–19.

Warhaft, Z. (1984). The interference of thermal fields from line sources in grid turbulence. *J. Fluid Mech.*, 144:363–387.

Waterson, N. and Deconinck, H. (2007). Design principles for bounded higher-order convection schemes–a unified approach. *J. of Comp. Phys.*, 224:182–207.

Xie, Z., Hayden, P., Voke, P. R. and Robins, A. G. (2004). Large-eddy simulation of dispersion: comparison between elevated and ground-level sources. *J. Turbulence*, 5:1–16.

Yee, E., Gailis, R. M. and Wilson, D. J. (2003). The interference of higher-order statistics of the concentration field produced by two point sources according to a generalized fluctuating plume model. *Boundary-Layer Meteorol.*, 106:297–348.

Table 1: Summary of test cases.

Case	Re_τ	Source separation (d)	Source size
1	180	0.066δ	0.014δ
2	180	0.131δ	0.014δ
3	180	0.295δ	0.014δ
4	180	0.558δ	0.014δ
5	395	0.049δ	0.007δ
6	395	0.115δ	0.007δ
7	395	0.279δ	0.007δ
8	395	0.541δ	0.007δ

Table 2: Summary of grid resolutions. Nx, Ny and Nz represent the number of grid nodes in the x-, y-, and z-directions, respectively. Δy^+_{min} and Δy^+_{max} are the minimum and maximum grid resolutions in the wall-normal direction.

Re_τ	$Nx \times Ny \times Nz$	Δx^+	Δz^+	Δy^+_{min}	Δy^+_{max}
180	$256 \times 128 \times 192$	8.8	3.9	0.03	4.6
395	$512 \times 256 \times 384$	4.8	3.2	0.03	2.4

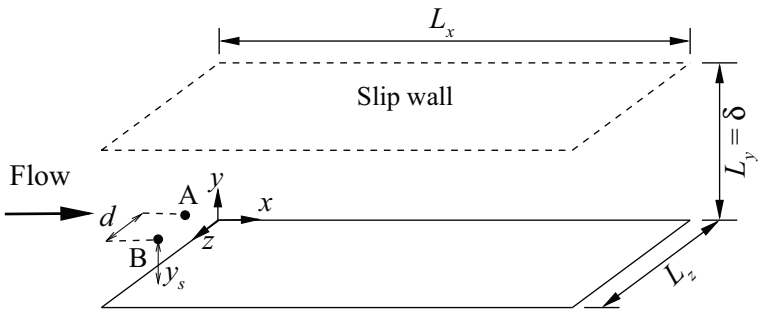

Fig. 1. Schematic of the computational domain of the open-channel flow. The two point sources positioned at A and B are separated in the spanwise direction by a distance d and are at height y_s above the lower (solid) channel wall.

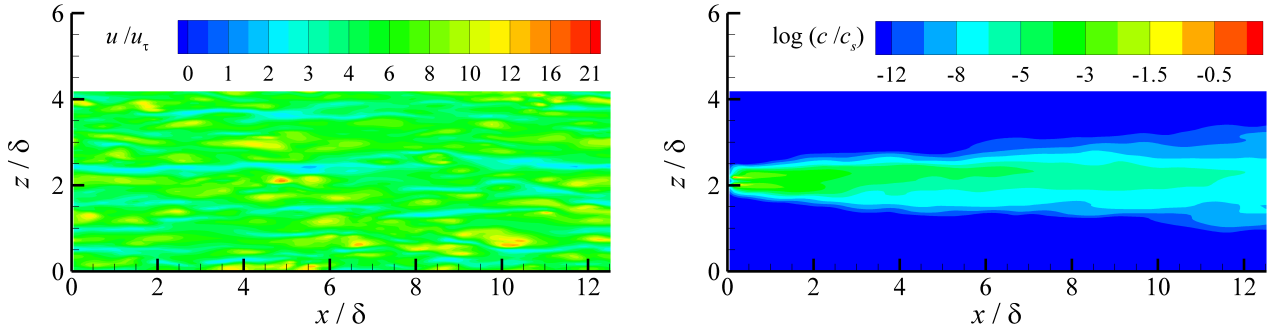

(a) Instantaneous streamwise velocity field

(b) Instantaneous scalar field when two sources are active

Fig. 2. Snapshots of the instantaneous streamwise velocity and concentration fields for case 4 on the x-z plane located at source height ($y_s^+ = 5$).

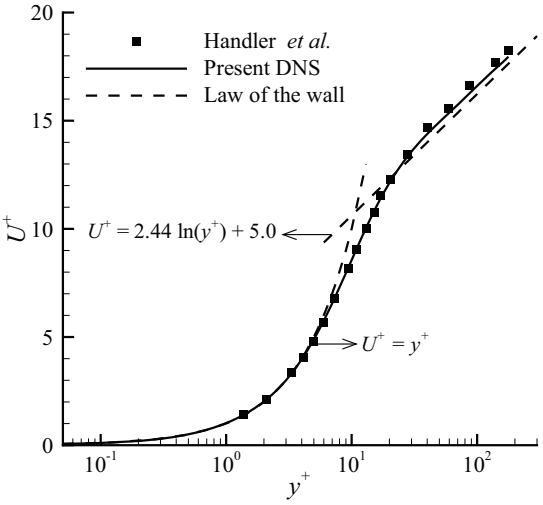

(a) Mean streamwise velocity ($Re_\tau = 180$)

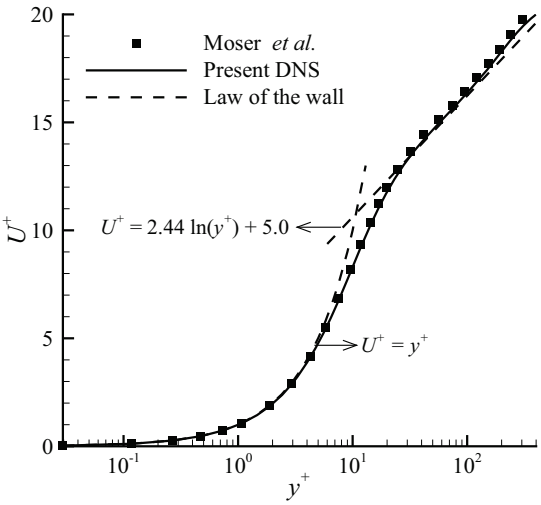

(b) Mean streamwise velocity ($Re_\tau = 395$)

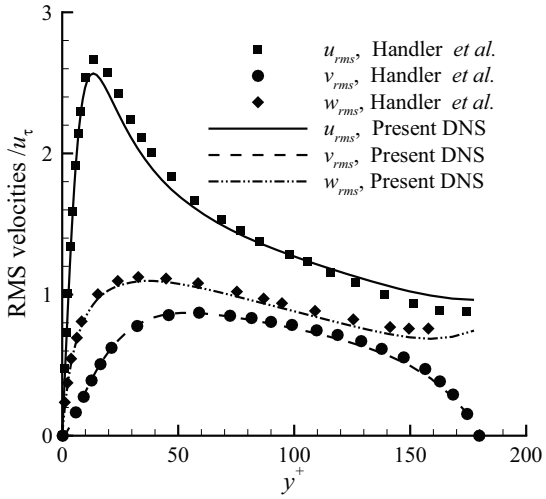

(c) RMS velocities ($Re_\tau = 180$)

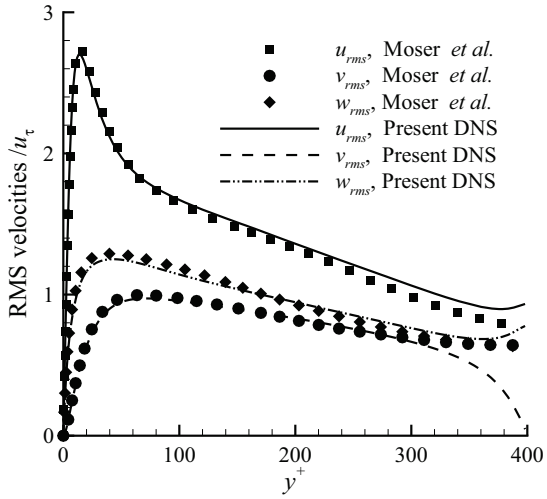

(d) RMS velocities ($Re_\tau = 395$)

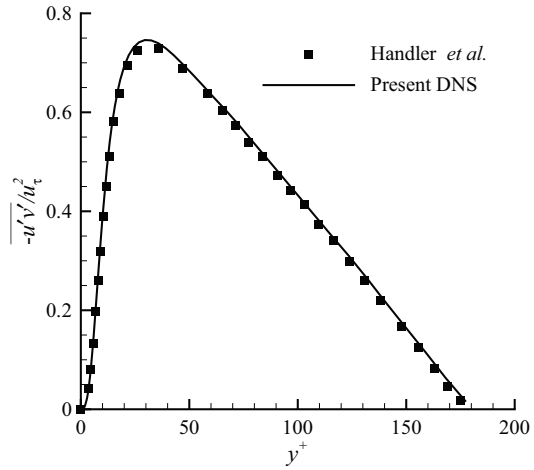

(e) Reynolds shear stress ($Re_\tau = 180$)

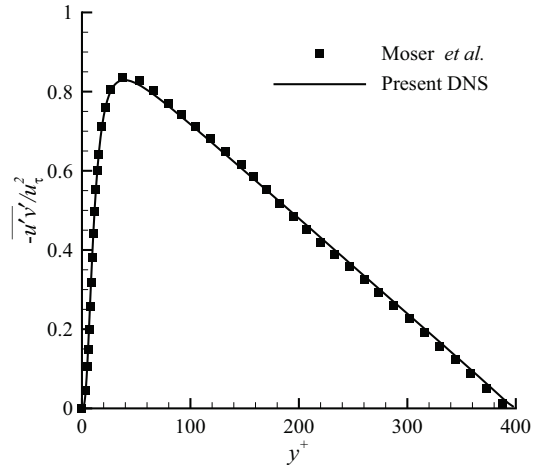

(f) Reynolds shear stress ($Re_\tau = 395$)

Fig. 3. Comparison of present DNS predictions of the velocity statistics of an open-channel flow against reported DNS data of Handler *et al.* (1999) for an open-channel flow and those of Moser *et al.* (1999) for a plane-channel flow. All flow statistics are non-dimensionalized using the wall friction velocity u_τ.

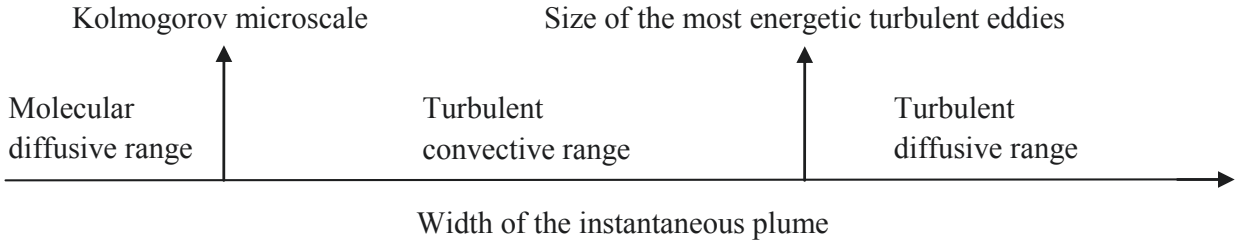

Fig. 4. The relative width of the instantaneous plume in the different regimes of plume development.

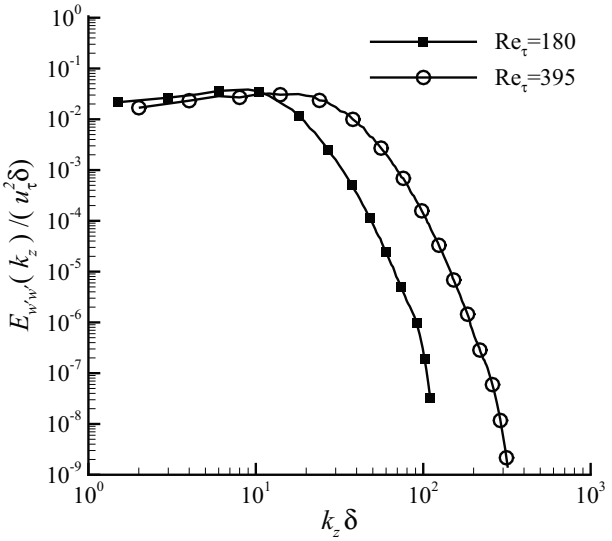

(a) Velocity spectra plotted against the spanwise wavenumber

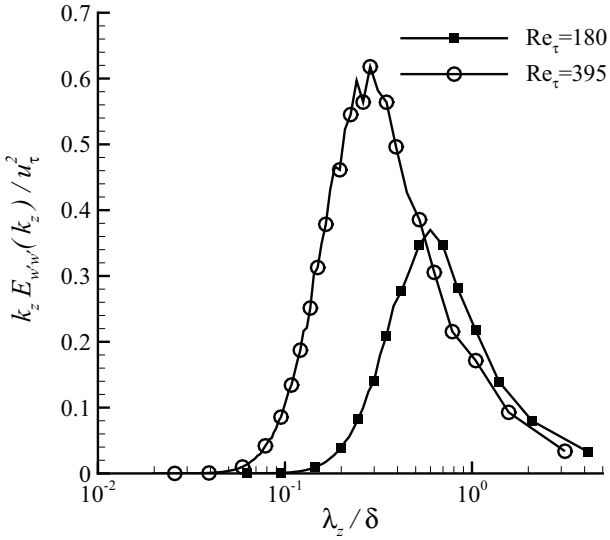

(b) Pre-multiplied velocity spectra plotted against spanwise wavelength

Fig. 5. Spanwise velocity spectra and pre-multiplied spectra at $y_s^+ = 5$.

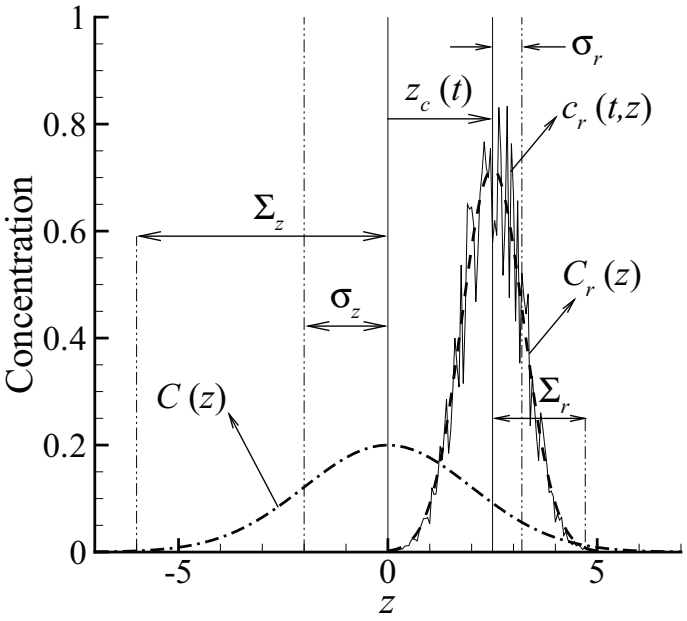

Fig. 6. Schematic of the plume scales.

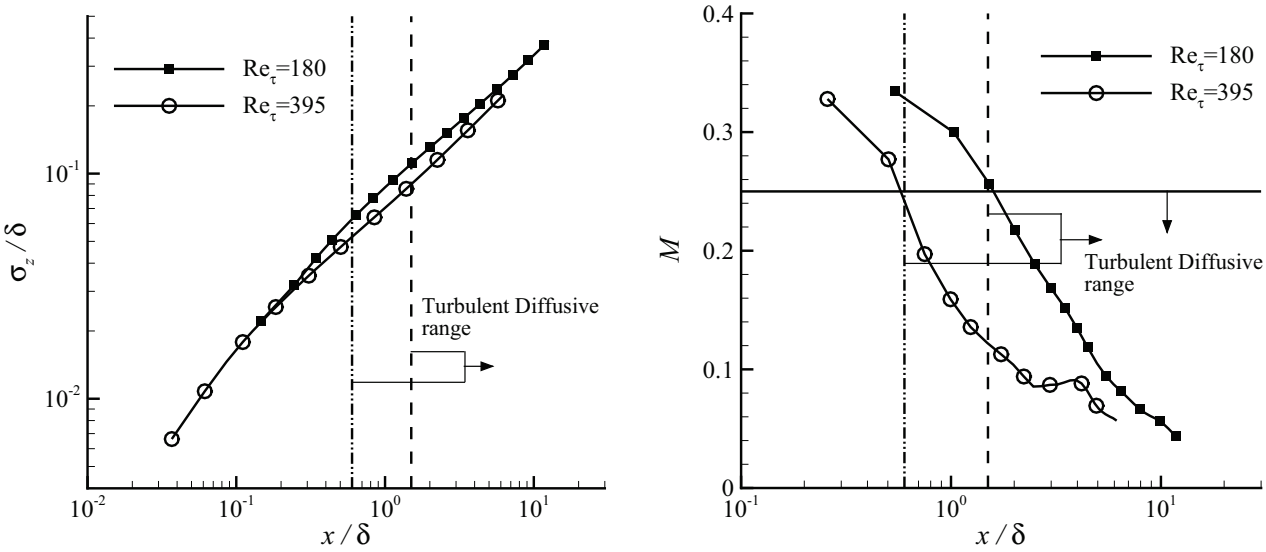

(a) Non-dimensionalized lateral mean plume dispersion

(b) Meandering ratio

Fig. 7. Streamwise variation of the non-dimensionalized lateral mean plume dispersion (σ_z/δ) and meandering ratio ($M = \sigma_c^2/\sigma_r^2$) at source height. The dashed and dash-dot-dotted vertical lines show the locations where the width of the instantaneous plume first reaches the size of the most energetic turbulent eddies for $Re_\tau = 180$ and 395, respectively.

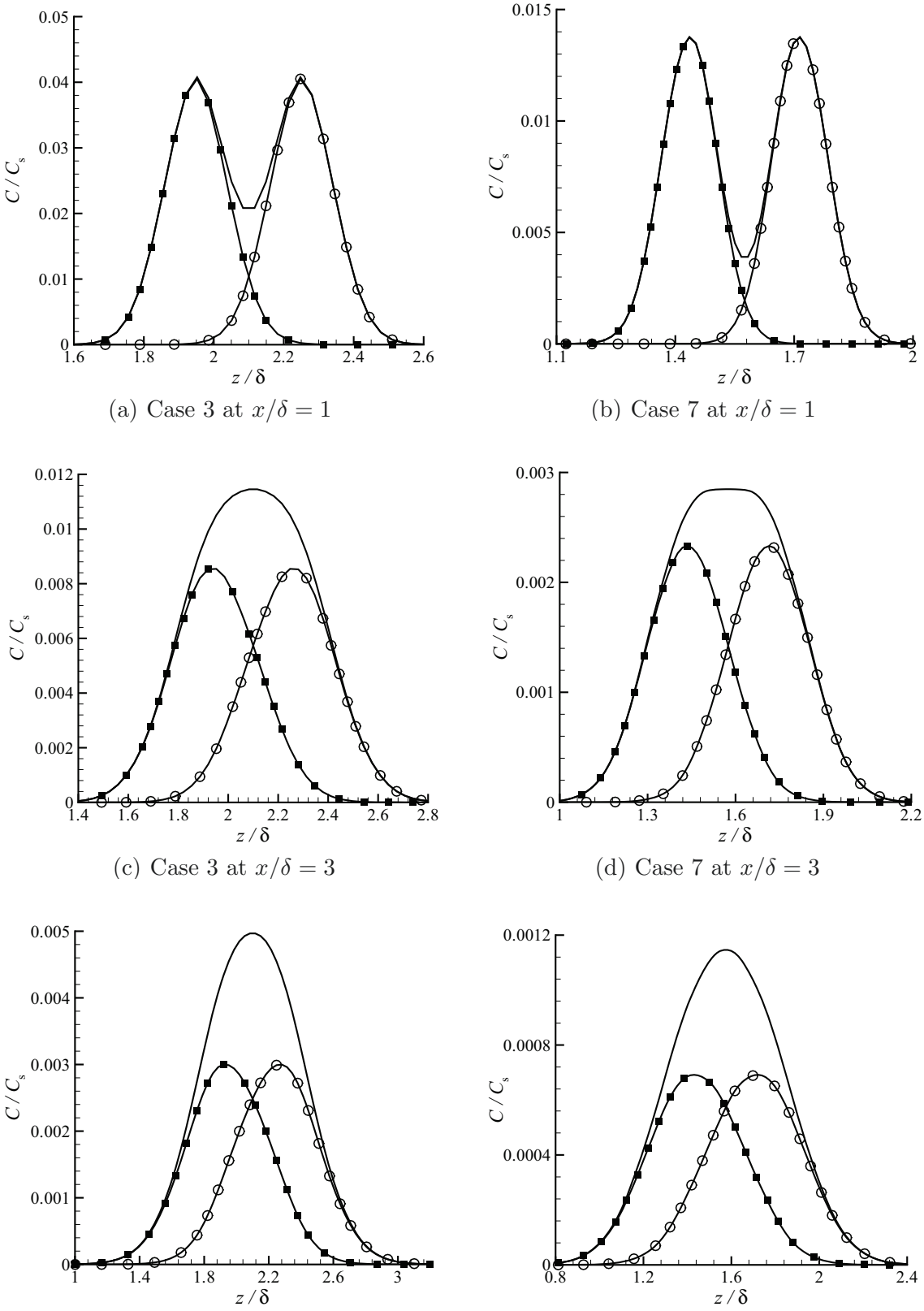

(a) Case 3 at $x/\delta = 1$

(b) Case 7 at $x/\delta = 1$

(c) Case 3 at $x/\delta = 3$

(d) Case 7 at $x/\delta = 3$

(e) Case 3 at $x/\delta = 6$

(f) Case 7 at $x/\delta = 6$

Fig. 8. Lateral profiles of the mean concentration for the source at A (■), for the source at B (◯), and for both sources (solid line) at three streamwise locations.

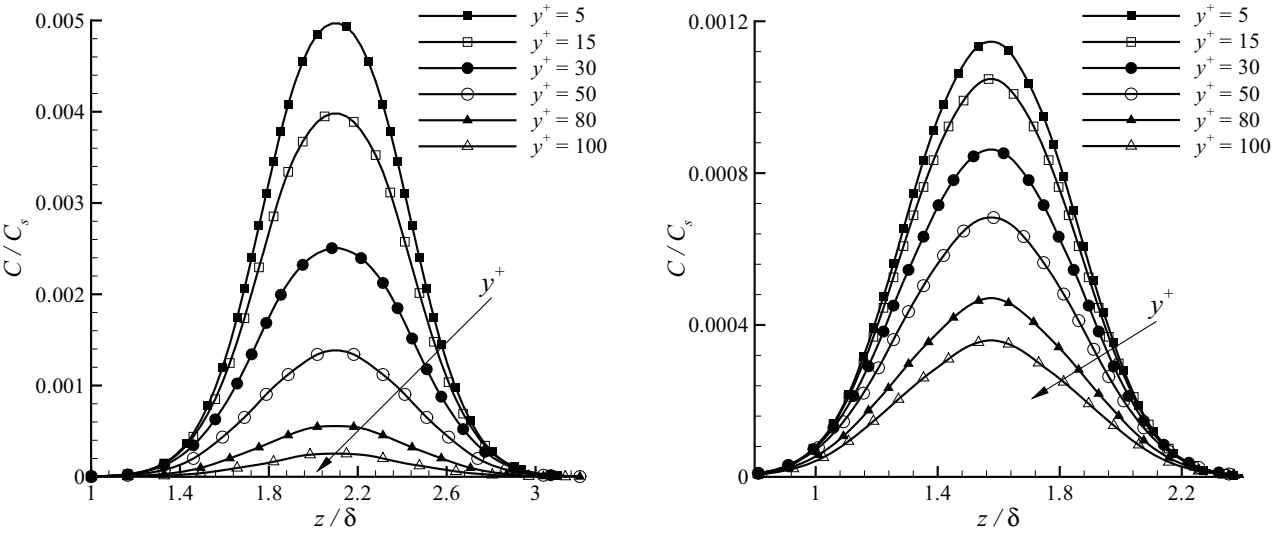

(a) Case 3 (b) Case 7

Fig. 9. Lateral profiles of the total mean concentration for different y^+ values at $x/\delta = 6$. The arrow points to the increasing direction of y^+.

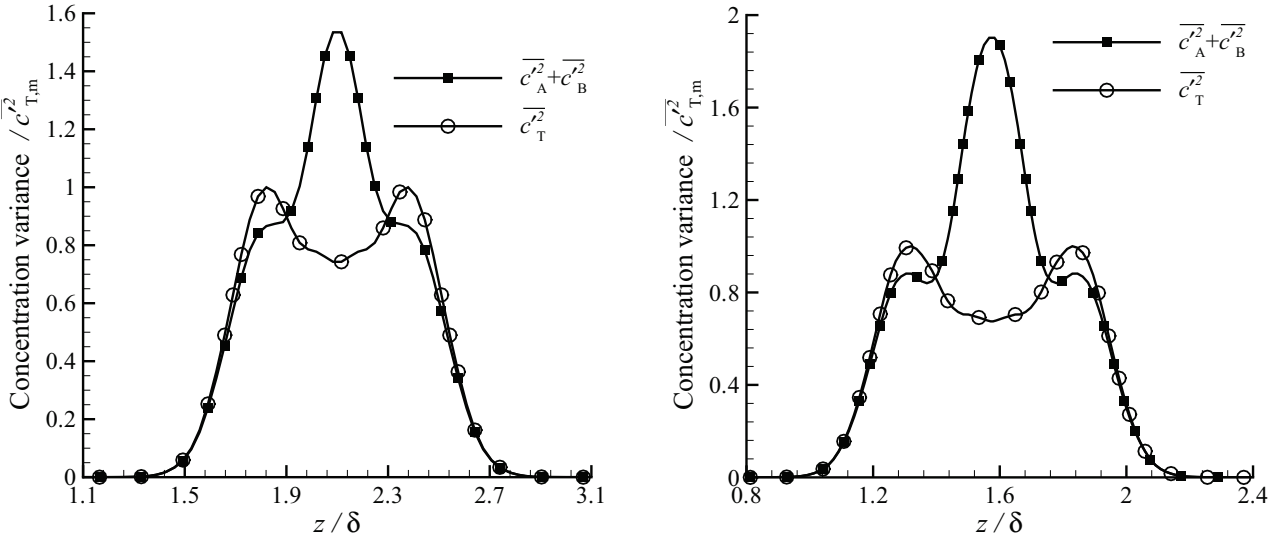

(a) Case 3 (b) Case 7

Fig. 10. Lateral profiles of the variance of concentration fluctuations at $x/\delta = 4$.

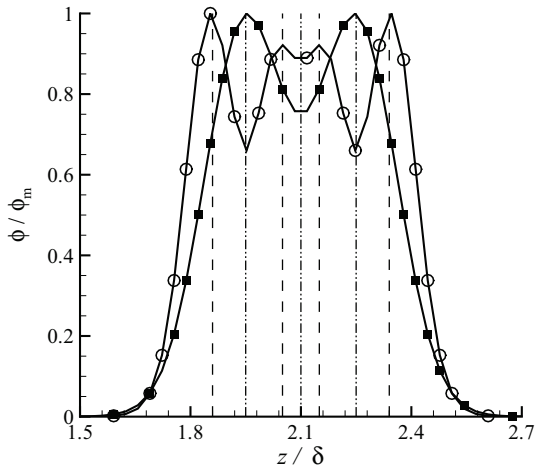

(a) Case 3 at $x/\delta = 2$

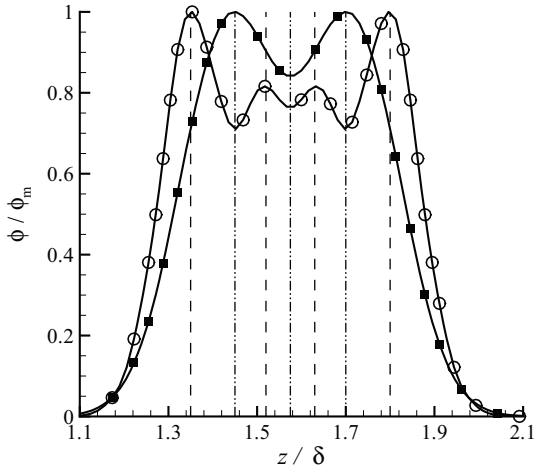

(b) Case 7 at $x/\delta = 2$

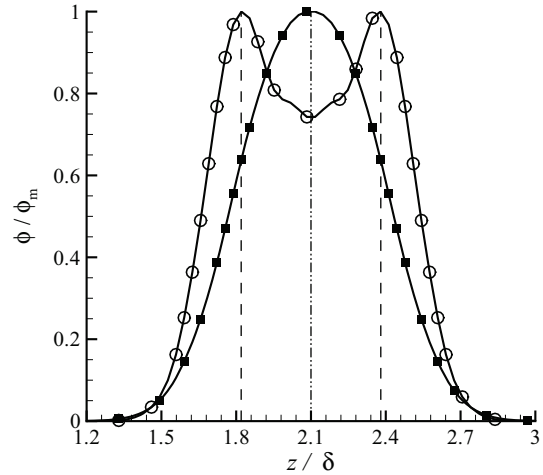

(c) Case 3 at $x/\delta = 4$

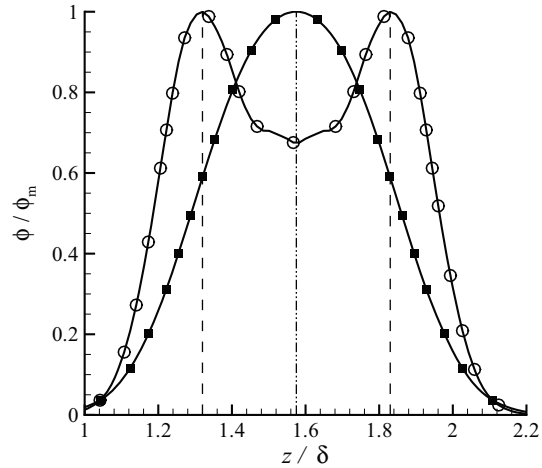

(d) Case 7 at $x/\delta = 4$

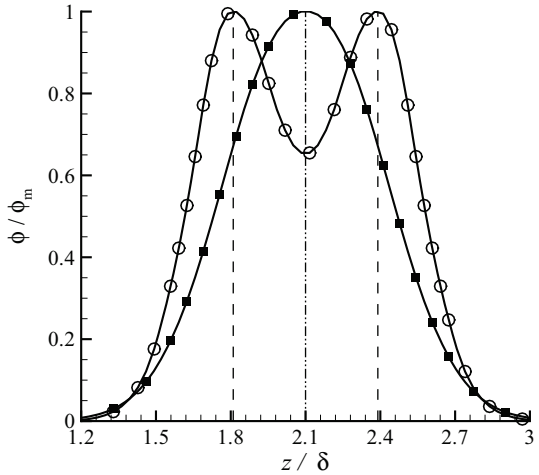

(e) Case 3 at $x/\delta = 6$

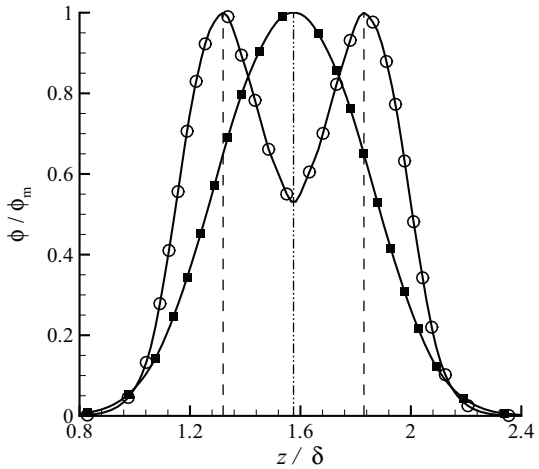

(f) Case 7 at $x/\delta = 6$

Fig. 11. Lateral profiles of the total mean concentration C_T (■) and the variance of concentration fluctuations of the total plume $\overline{c_T'^2}$ (◯). Straight vertical dashed and dash-dot-dotted lines indicate the locations of the local maxima of the absolute total mean concentration gradient and the locations of the local extrema of the mean concentration profile, respectively. Symbol ϕ represents either C_T or $\overline{c_T'^2}$.

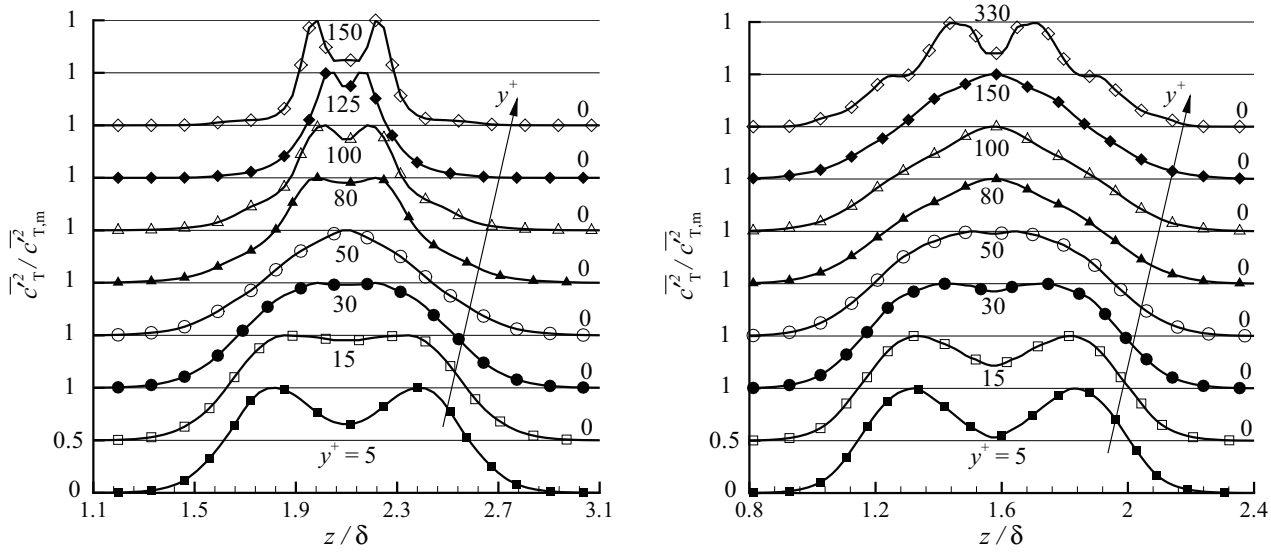

(a) Case 3 (b) Case 7

Fig. 12. Lateral profiles of the variance of concentration fluctuations for different y^+ values at $x/\delta = 6$. The arrow points to the increasing direction of y^+.

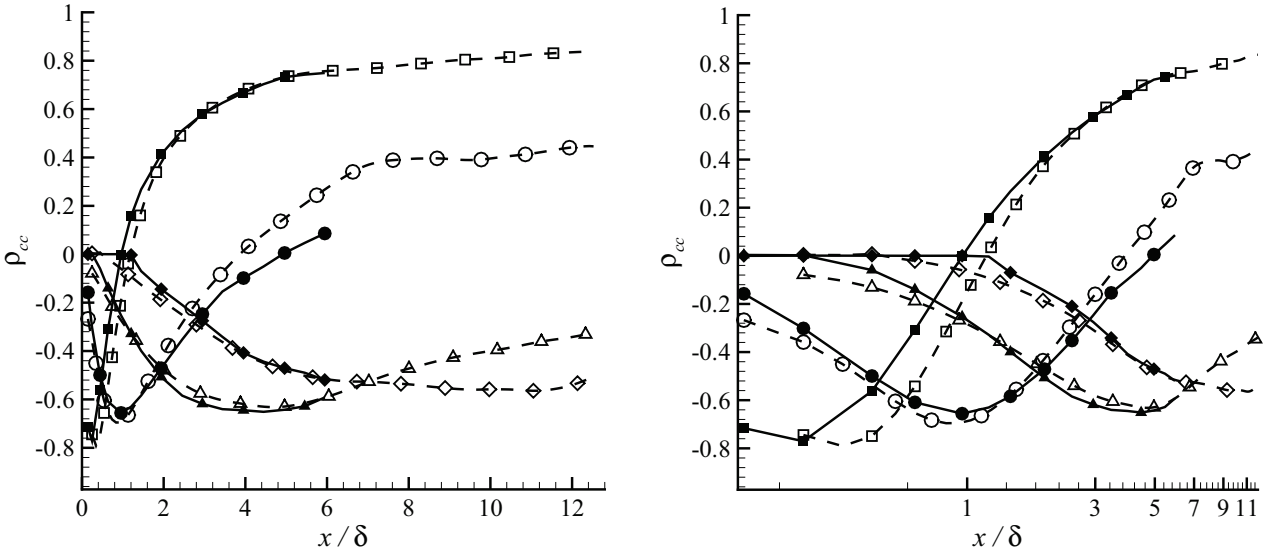

(a) Linear-linear (b) Log-linear

Fig. 13. Streamwise variation of the cross correlation ρ_{cc} in the midplane along the spanwise direction between the plumes at source height. Cases 1 (□), 2 (◯), 3 (△), 4 (♢), 5 (■), 6 (●), 7 (▲), and 8 (♦).

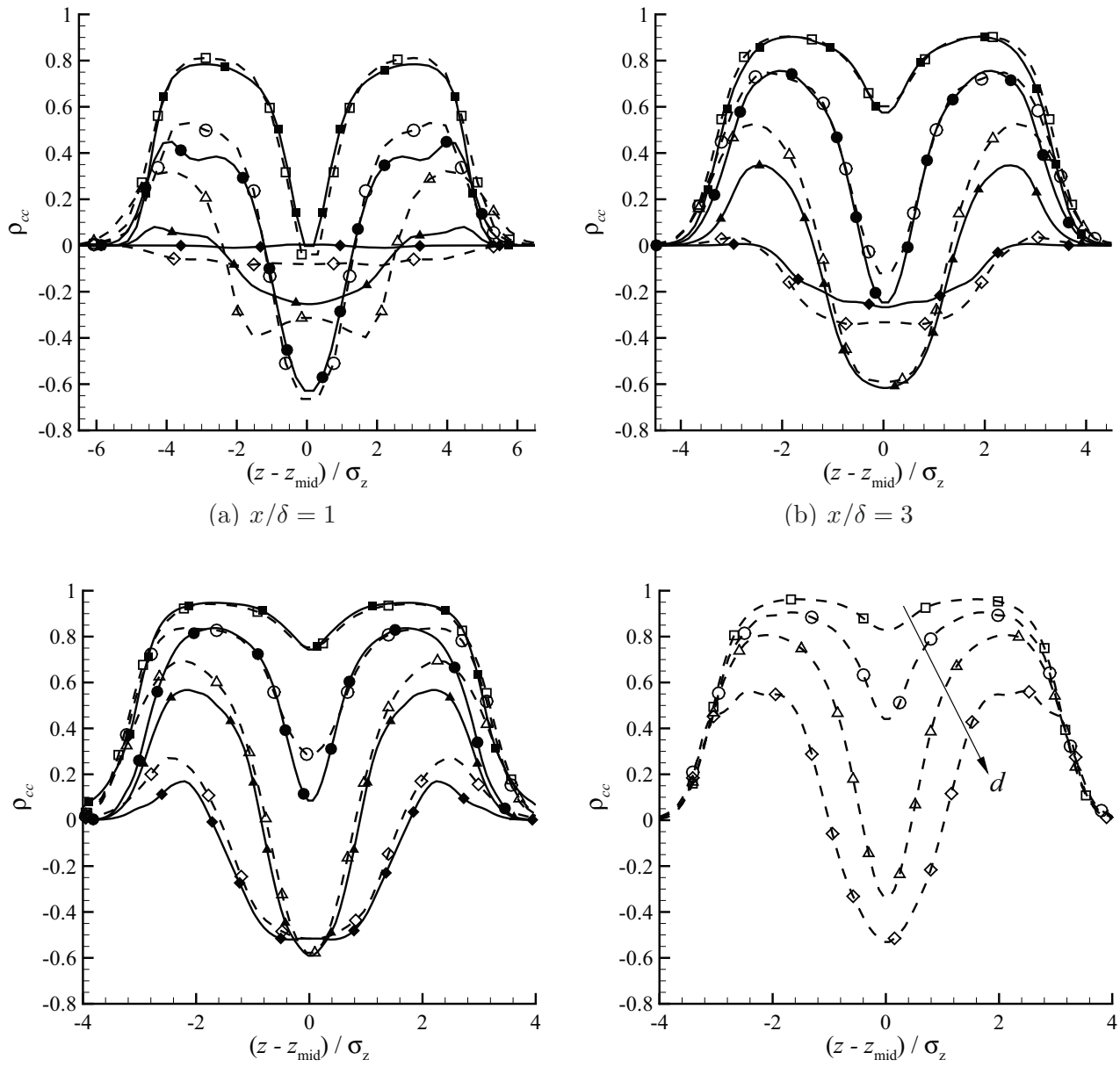

(a) $x/\delta = 1$ (b) $x/\delta = 3$

(c) $x/\delta = 6$ (d) $x/\delta = 12$

Fig. 14. Lateral profiles of the cross correlation ρ_{cc} at source height. Cases 1 (□), 2 (◯), 3 (△), 4 (◇), 5 (■), 6 (●), 7 (▲), and 8 (♦).

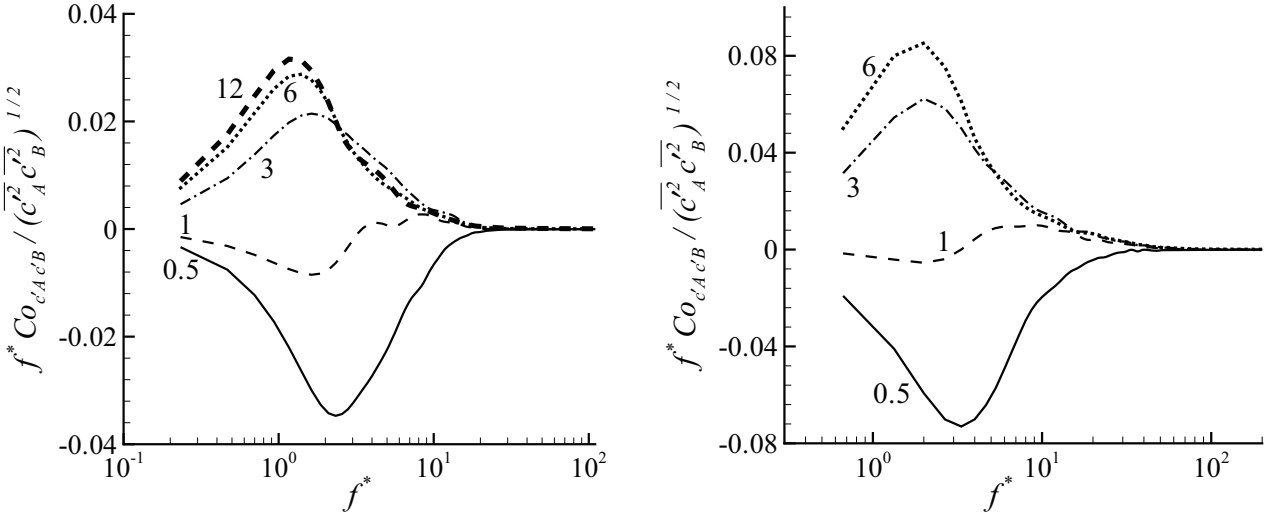

(a) Case 1 (small source separation, $Re_\tau = 180$) (b) Case 5 (small source separation, $Re_\tau = 395$)

Fig. 15. The pre-multiplied co-spectrum of two plumes for cases 1 and 5 obtained at the midpoint between the two plumes and at source height, for $x/\delta = 0.5$ (solid line), 1 (thin dashed line), 3 (dash-dotted line), 6 (dotted line) and 12 (thick dashed line).

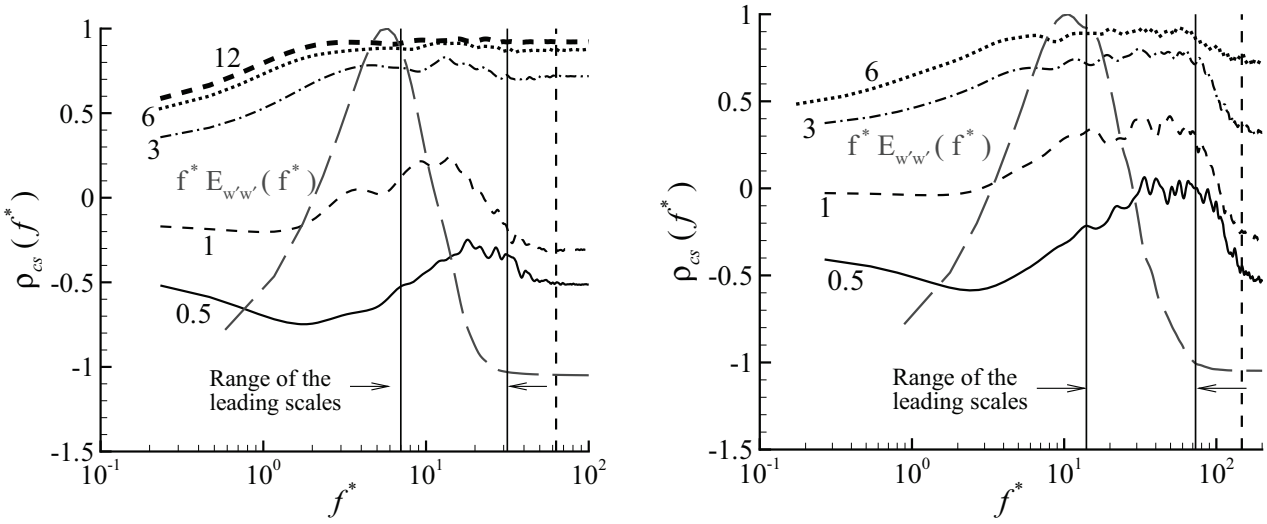

(a) Case 1 (small source separation, $Re_\tau = 180$) (b) Case 5 (small source separation, $Re_\tau = 395$)

Fig. 16. The coherency spectrum ρ_{cs} of two plumes for cases 1 and 5 obtained at the midpoint between the two plumes and at source height, for $x/\delta = 0.5$ (thin solid line), 1 (dashed line), 3 (dash-dotted line), 6 (dotted line) and 12 (thick dashed line). The straight vertical dashed line shows the frequency corresponding to the Kolmogorov scale. The long dashed curve shows the pre-multiplied energy spectrum $f^*E_{w'w'}$ of velocity fluctuations in the spanwise direction. The pre-multiplied energy spectrum $f^*E_{w'w'}$ is used here for identifying the frequency corresponding to the most energetic eddies (through its peak location), and its magnitude has been re-scaled arbitrarily in order to fit in the figure panel.